Tebentafusp elicits on-target cutaneous immune responses driven by cytotoxic T-cells in uveal melanoma patients

Ramon Staeger[#] [1,2], Aizhan Tastanova[#*] [1,2], Adhideb Ghosh [3], Nicola Winkelbeiner [1], Prachi Shukla [1,2], Isabel Kolm [1,2], Patrick Turko [1,2], Adel Benlahrech [4], Jane Harper [4], Anna Broomfield [4], Antonio Camera [4], Marianna Ambrosio [1], Veronika Haunerdinger [1,2], Phil Cheng [1,2], Egle Ramelyte [1,2], James P. Pham [5,6], Stefanie Kreutmair [7,8], Burkhard Becher [7], Mitchell P. Levesque [1,2], Reinhard Dummer [1,2], Barbara Meier-Schiesser*[†] [1,2]

shared authorship

* Corresponding authors and [†]lead contact

1: Department of Dermatology, University Hospital Zurich, Zurich, Switzerland

2: Medical Faculty, University of Zurich, Zurich, Switzerland

3: Functional Genomics Center Zurich, University of Zurich and ETH Zurich, 8057 Zurich, Switzerland

4: Immunocore Ltd, 92 Park Dr, Abingdon-on-Thames, OX14 4RY, UK

5: Department of Medical Oncology, The Kinghorn Cancer Centre, St Vincent's Hospital Sydney, Darlinghurst, NSW, Australia

6: School of Clinical Medicine, UNSW Medicine and Health, Sydney, NSW, Australia

7: Institute of Experimental Immunology, University of Zurich, 8057 Zurich, Switzerland

8: Department of Medical Oncology and Hematology, University Hospital Zurich, Zurich, Switzerland

Correspondance: barbara.meier-schiesser@usz.ch

Rämistrasse 100, 8901 Zurich, Switzerland

aizhan.tastanova@usz.ch

Wagistrasse 18, 8952, Schlieren, Switzerland

Abstract

Background: Tebentafusp is the first T-cell receptor-based bispecific protein approved for clinical use in HLA-A*02:01+ adult patients with unresectable/metastatic uveal melanoma. It redirects T-cells toward gp100-expressing target cells, frequently inducing skin-related early adverse events.

Methods: This study investigated immunological and cellular responses using single-cell and spatial analysis of skin biopsies from patients with metastatic uveal melanoma treated with tebentafusp.

Results: 81.8% of patients developed acute cutaneous adverse events, which correlated with improved survival. Multimodal analysis revealed a brisk infiltration of CD4+ and CD8+ T-cells, while melanocyte numbers declined. Single-cell RNA-sequencing revealed T-cell activation, proliferation, and IFN-γ/cytotoxic gene upregulation. CD8+ T-cells co-localized with melanocytes and upregulated LAG3, suggesting potential for combination therapies with tebentafusp. Melanocytes upregulated antigen presentation and apoptotic pathways, while pigmentation gene expression decreased. However, gp100 remained stably expressed.

Conclusion: Sequential skin biopsies enable *in vivo* pharmacodynamic modeling of tebentafusp, offering insights into immune activation, toxicity, and treatment response. Examining the on-target effects of bispecifics in tissues amenable to longitudinal sampling enhances our understanding of toxicity and therapeutic escape mechanisms, guiding strategies for treatment optimization.

Funding: Cancer Research Foundation, Swiss National Science Foundation (323630_207029, 733 310030_170320, 310030_188450, CRSII5_183478), Iten-Kohaut foundation, European Research Council no. 882424, University Priority Project translational cancer research of the UZH, UZH PostDoc grant (K-85810-02-01).

Introduction

Tebentafusp is approved for HLA-A*02:01+ adult patients with unresectable or metastatic uveal melanoma (mUM) and is the first T-cell receptor (TCR)-based agent in clinical use (1). It is based on the ImmTAC (Immune mobilising monoclonal T-cell receptors Against Cancer) platform (2), and targets the melanoma-associated antigen gp100 through a soluble TCR fused to an anti-CD3 T-cell mobilizing domain (3). Unlike antibody-based treatments that are generally directed against membrane-bound proteins, the TCR-based bispecifics enable access to the vast pool of intracellular antigens as therapeutic targets (4).

The TCR is engineered for high affinity binding of the gp100-derived 9-mer peptide YLEPGPVTV in the context of HLA-A*02:01 (5), the most common allele at this locus (6). gp100 is a melanocyte-lineage antigen, plays an essential role in melanin pigment biosynthesis (7), with gp100 peptide-HLA (pHLA) complexes presented on the surface of normal melanocytes and on melanoma cells (8). Due to the high affinity of the TCR, cells with low target density on their surface are efficiently recognized and bound with a long half-life in a first step (4). The anti-CD3 single-chain variable fragment was optimized to have a lower affinity, therefore T-cell activation would follow pHLA recognition and not vice versa (2). Finally, prolonged engagement of CD3 receptor on T-cells induces polyclonal activation of T-cells, irrespective of their cognate TCR specificity, resulting in release of interferon-γ (IFN-γ) and granzyme B (GZMB) that mediate target cell death dependent on gp100 pHLA abundance on the target cell surface (8, 9).

Uveal melanoma (UM) originates from melanocytes in the choroid or less commonly in the ciliary body or iris of the eye and frequently metastasizes to the liver (10). Approximately 50% of patients with UM develop metastatic disease, for which the prognosis is poor, with liver-directed therapies or systemic treatments with chemotherapies or Immune checkpoint inhibitors (ICI) showing limited survival benefits (11). In a pivotal phase III trial, despite relatively low objective response rates of 9%, treatment with tebentafusp resulted in a significantly longer overall survival compared to the investigators' choice control group (the 1-year and 3-year OS rate in the tebentafusp arm was 73% and 27%, respectively,

versus 59% and 18% in the control arm) (1, 12). As the first treatment to demonstrate a survival benefit in mUM, tebentafusp has become the new standard of care for patients with the HLA-A*02:01 allele.

Notably, the majority of patients treated with tebentafusp in the phase III trial developed cutaneous adverse events (cAE) such as “rash” (83%), pruritus (69%) and pigmentation disorders (45%) (1, 13). “Rash” was used as a composite term for a list of cAE, including erythematous, maculopapular and vesicular eruptions. These were mostly low grade, with none resulting in discontinuation of tebentafusp treatment, and showed a very early onset (1, 13). cAE are likely an off-tumor/on-target effect from tebentafusp-mediated recruitment of T-cells to gp100 expressing melanocytes in the skin (14). We reasoned that sequential skin biopsies may serve as an *in vivo* pharmacodynamic model to study tebentafusp-induced responses such as T-cell activation, effects on target cells, and contributions of bystander cells. Given that cutaneous inflammatory responses against melanocytes may mirror processes in the tumor microenvironment under tebentafusp, research on cAE could offer insights into the mechanisms of action and treatment resistance associated with TCR-based bispecifics.

Results

In this study, the cellular and molecular dynamics of cAE in patients with mUM receiving tebentafusp were analyzed. Skin biopsies were collected from 11 patients at baseline and at the onset of an acute cAE (acAE) on tebentafusp treatment (or from unaffected skin for patients with no acAE) (**Figure 1A**). Additional lesional skin samples from vitiligo-like pigmentation disorder (VLPD) were collected later on treatment from 5 patients (**Figure 1A**). Using multiplex immunohistochemistry (mIHC), and single-cell RNA sequencing (scRNA-seq), a comprehensive assessment of the cellular pharmacodynamics in the skin in response to tebentafusp was conducted.

Tebentafusp causes acute cutaneous adverse events

cAE to tebentafusp occurred in 9 of 11 patients (81.8%), most commonly as acute skin eruption 12-48 hours after the first three infusions, presenting as diffuse erythematous sunburn-like (n=7), macular (n=1) or maculopapular (n=1) manifestations of grade 1-2 (**Figure 1B-C, Supplementary Table 1**), in line with previous reports (1, 15). Skin eruptions were frequently accompanied by pruritus (n=6, 54.4%)

(**Figure 1B-C, Supplementary Table 1**). Facial edema and a single bulla were present in three (27.3%) and one patient, respectively **(Figure 1B-C, Supplementary Table 1)**. In all cases, acAE were transient, responsive to oral antihistamines and topical steroids and resolved by the next infusion a week later, apart from occasional superficial desquamation. Regarding delayed cAE, VLPD occurred in 7 patients (63.6%), with a median onset of 192 days (range 85-275 days) following tebentafusp initiation (**Figure 1B-C, Supplementary Table 1**). Notably, all instances of VLPD were preceded by an acAE. Cytokine-release syndrome (CRS) was diagnosed in 72.7% of cases, with 62.5% being grade 2 (per CTCAE v5) and responding well to intravenous fluids and antipyretic medication, while the remaining cases were grade 1. 3 or higher adverse events were not reported and no patient discontinued treatment due to toxicity.

Acute cutaneous adverse events correlate with outcome

After a median follow-up duration of 24.4 months (range 14.7-26.2 months), median progression-free survival (PFS) was 2.2 months (96% CI: 2.0 to not reached) (**Supplementary Figure 1A**) and the 1-year overall survival (OS) rate was 81.8% (95% CI: 61.9 to 100), while median OS was not reached (**Supplementary Figure 1B**). Development of acAE correlated with significantly longer OS (p=0.0004) (**Figure 1D**). However, occurrence of acAE correlated with baseline serum Lactate Dehydrogenase (LDH) levels, an important prognostic marker (**Figure 1E and F**). In a multivariate Cox proportional hazards model controlling for LDH, age and sex, acAE was not found to be an independent predictor of PFS or OS.

Tebentafusp induces T-cell infiltration into the dermo-epidermal junction

Baseline skin biopsies were collected from all patients (n=11) prior to tebentafusp initiation. On-treatment biopsies were taken from acAE lesional skin (n=9) or from clinically unaffected skin in cases without acAE (n=2). Blinded histological evaluation of paired baseline and lesional skin biopsies (8 patients) was assessed by a certified dermatopathologist (**Figure 1G-H**). The presence of interface dermatitis, defined as infiltration of T-cells along the dermo-epidermal junction, cytoplasmic vacuolization of the basal epidermal layer and apoptotic keratinocytes was a constant finding in acAE samples (p=0.012, compared to baseline) (**Figure 1H**) and was absent in non-acAE samples

(**Supplementary Figure 1C and D**). This supports the proposed mechanism of tebentafusp-induced skin inflammation via T-cell recruitment against gp100+ melanocytes in the basal epidermis, leading to bystander keratinocyte damage (1, 16, 17). Furthermore, increased dermal T-cells in a perivascular distribution were observed ($p<0.031$) (**Figure 1H**). In summary, tebentafusp-induced acAEs involved T-cell infiltration.

CD4+ and CD8+ T-cells increase and melanocytes decrease in lesional skin

Due to skin inflammation in tebentafusp-induced acAE (**Figures 1B, C, G and H**) we investigated the composition, spatial distribution, and co-localization of the immune infiltrate. For this purpose, mIHC was performed on paired skin biopsies at baseline (n=9), acAE onset (n=9), and from VLPD (n=5) (**Figure 2A**). Spectral unmixing and single-cell Leiden clustering detected six clusters that were annotated as CD4+ T-cells, CD8+ T-cells, CD68+ macrophages, pan-cytokeratin (PanCK)+ keratinocytes and Melan-A+/SOX10+ (cytoplasmic and nuclear markers) melanocytes (**Figure 2A-B**).

Proportions of CD4+ and CD8+ T-cells significantly increased in acAE compared to baseline (p-adj=0.026 and p-adj<0.0003, respectively), while in VLPD lesions, T-cell proportions were heterogeneous, with normalization in most patients but a further increase in a few patients (not significant) (**Figure 2C**). Macrophage proportions were not markedly altered in acAE or VLPD compared to baseline (**Figure 2C**). Keratinocytes were significantly reduced in acAE (p-adj=0.017), as expected in the case of interface dermatitis with epidermal vacuolization (**Figure 2C**). Indeed, epidermal cell swelling in histology ($p<10^{-15}$, Cohen's *d*=0.3) (**Figure 2D**) and increased epidermal cell death marked by TUNEL staining ($p<10^{-15}$, odds ratio 12.2) were observed (**Figure 2E, Supplementary Figure 1E**) (18). Melanocyte proportions were decreased in acAE (p-adj=0.016) and remained below baseline levels in 4 out of 5 VLPD lesions (not significant) (**Figure 2C**). In summary, both CD4+ and CD8+ T-cells increased in acAE under tebentafusp, while melanocytes and keratinocytes decreased.

CD8+ T-cells are enriched in close proximity to melanocytes

Immune cell effector functions depend on spatial proximity to the target cell; for instance, CD8+ T-cell cytotoxic activity requires cellular juxtaposition. Using mIHC, the coordinates and spatial relationships of the immune cells relative to the epidermis were mapped **(Figure 2F)**. Next, as gp100+ cells are targeted by tebentafusp-mediated T-cell redirection, the density of the immune cells was surveyed in incremental circles of 10 µm (1-2 cell widths) away from each melanocyte. In 4 of 9 patients with acAE, CD8+ T-cells showed the highest enrichment in the immediate proximity of the melanocytes, in contrast to CD4+ T-cells and macrophages which were distributed more uniformly across skin tissue **(Figure**

2G). In VLPD skin, spatial proximities of all three cell types to melanocytes were reduced compared to acAE, yet remained above baseline levels (**Figure 2G**). Thus, the CD8+ T-cells preferentially localized and persisted in the immediate vicinity of the melanocytes, which is a prerequisite for tebentafusp driven cytotoxic-effector functions.

Single-cell RNA sequencing reveals T-cell proliferation in the acAE skin

To further investigate the cellular and molecular dynamics of tebentafusp-induced skin inflammation, scRNA-seq was performed on paired baseline and acAE skin biopsies from 3 patients. After QC filtering (methods), a total of 23638 high quality cells (mean 3940 cells/sample) were available for downstream analysis.

Ten major skin cell types were detected: Keratinocytes (*KRT14*), melanocytes (*MITF*), lymphocytes (*CD2*), myeloid cells (*HLA-DRA, CD163*), fibroblasts (*COL1A1*), vascular endothelial cells (*CD93*), lymphatic endothelial cells (*FLT4*), pericytes (*PDGFRB*), smooth muscle cells (*ACTA2*), and glial cells (*MPZ*) (**Supplementary Figure 2**). The cell type composition was comparable with previous findings in skin (19). Interestingly, glial cells showed significantly reduced abundance in acAE compared to baseline (p-adj<$4x10^{-5}$).

The mechanism of action of the gp100-ImmTAC molecule tebentafusp is based on recruitment of CD3+ T-cells to gp100 expressing cells. Gp100 is a melanocyte-lineage antigen expressed by epidermal melanocytes, hence acAE was suggested to be an on-target/off-tumor effect (1, 13). For an in-depth analysis of the lymphocyte cluster, second-level clustering was performed which resulted in 7 subclusters of T and NK cells (**Figure 3A and B, Supplementary Figure 3 A and B**). The distribution of CD4+ and CD8+ expressing T-cells is shown in **Supplementary Figure 3C.** Subcluster 1 was marked by *CCR4* and *CCR6*, both skin-homing chemokine receptors (20–22) as well as the tissue-residency associated genes *VIM* and *ANXA1* (23, 24) (**Figure 3B**). This cluster contained both CD4+ and CD8+ T-cells (**Supplementary Figure 3D**). High expression of *IL7R* indicated a naive/resting memory T-cell phenotype (24–27). Subcluster 2 was marked by *CD69* and other markers of tissue-resident memory T-cells (TRM) such as *KLF6, ANKRD28,* and *NR4A1* (23, 28–32) while *S1PR1* and *CCR7* were low (33, 34). Subcluster 3 regulatory T-cells (Tregs) based on *FOXP3*, *CD4*, and *CTLA4*

expression (35). Subclusters 4 and 5 were marked by cytotoxic gene expression and separated into natural killer (NK) cells based on *KLRD1*, *XCL1*, *NKG7* (36, 37) and CD8+ cytotoxic T-cells (CTL) based on *CD8A*, *IFNG, GZMA* and *GZMB*. Subcluster 6 was marked by expression of *CD8A, CD8B* and the activation-related markers *IL2RA, IL32, ENO1,* and *ACTB* (24, 38, 39), therefore corresponding to activated CD8+ T-cells.

Subcluster 7 were proliferating T-cells (*MKI67*, *ASPM*, *PCNA*) (24) (**Figure 3B**), the proportion of which increased >7-fold in acAE (p-adj=0.00057) (**Figure 3C**). This proliferating T-cell cluster contained both CD4+ (16.9%) and CD8+ T-cells (26.2%) (**Figure 3D**). Proliferation of both CD4+ and CD8+ T-cells was replicated *in vitro* after co-culturing with gp100-expressing cells in the presence of gp100-ImmTAC (**Figure 3E**). The proliferation of T-cells in the skin on-treatment suggests that co-localization with epidermal gp100-expressing cells (**Figure 1G and 2G**) results in tebentafusp-mediated T-cell activation *in situ*.

IFN-γ and cytotoxic T-cell activity are increased in acAE

The Th1 cytokine (IFN-γ) is an important immunostimulatory and antitumor effector molecule. Increased systemic levels of IFN-γ were observed in patients within hours of tebentafusp infusion (3). *In vitro*, IFN-γ was predominantly secreted by CD8+ T-cells in response to gp100-ImmTAC. In line with this, CD8+ cytotoxic T-cells upregulated *IFNG* in the skin on-treatment, although not statistically significant (**Figure 3F**) (avg.log2FC=0.93). The frequency of IFN-γ expressing CD8+ cytotoxic T-cells increased 1.4-fold (from 6.9% to 9.5%, not significant) (**Figure 3G**) and the IFN-γ gene expression signature increased significantly (p-adj=2.6e-81, Cohen's *d* = 0.81) in acAE (**Figure 3H**).

Normal melanocytes exhibit lower gp100 expression compared to melanoma (40). To explore the potential of low gp100 levels to activate T-cell responses, mirroring the skin conditions, increasing concentrations of gp100 peptide were pulsed onto gp100-negative cells. IFN-γ (**Figure 3I**) secretion occurred at very low gp100 peptide concentration of 1-10 nM, which likely represents the gp100 peptide range for healthy melanocytes (8, 41). IFN-γ secretion was gp100 level dependent, suggesting why lower T-cell responses were observed against melanocytes compared to melanoma cells *in vitro* (8, 42). To investigate the relationship between gp100 levels and IFN-γ-mediated cytotoxicity, normal

human epidermal melanocytes (NHEMs) were co-cultured with effector cells at varying tebentafusp concentrations. Gp100-positive and gp100-negative melanoma cell lines were used as positive and negative controls, respectively. Tebentafusp-dependent release of GZMB and IFN-γ was observed in co-cultures with NHEMs (**Figure 3J**), with a more pronounced effect in gp100-positive melanoma cells. Higher response is likely due to two-fold higher number of surface gp100-epitope counts in melanoma cells compared to NHEMs. Consistent with previous reports (42), no GZMB or IFN-γ release was detected in gp100-negative cells (**Figure 3J**). Together, these results demonstrate a gp100 level dependent increase in IFN-γ activity in acAE skin upon gp100-ImmTAC treatment.

A strong overexpression of glycolysis genes across T subclusters (p-adj=2.4e-115, Cohen's *d* = 0.99) (**Figure 3K and L**) suggested a broad activation of T-cells (43, 44), further supported by the marked downregulation of *IL7R* (avg.Log2FC=-1.2, p-adj=2.01E-80) (**Supplementary Figure 3E**), a marker of naive T-cell phenotypes that is downregulated following TCR stimulation (27, 45, 46). Upregulation of cytotoxic gene expression was observed (p-adj=2.5e-62, Cohen's *d* = 0.72) (**Figure 3M**) in the CD8+ T-cell subclusters, the NK cells, and the proliferating T-cells (**Figure 3N**).

CD8+ T-cells upregulate the LAG3 in acAE

Besides T-cell activation, immunoregulatory mechanisms were also observed in acAE skin. The alpha subdomain of the high-affinity IL-2 receptor *IL2RA* (CD25) is a marker of activated T-cells (47), and was upregulated in the proliferating and the CD8+ IL2RA+ T-cells (p-adj=3.60E-11) (**Figure 3O**). *IL2RA* is also implicated in immunoregulatory functions exerted by Tregs (48), where *IL2RA* was upregulated on tebentafusp treatment (**Figure 3O**). Furthermore, the immune checkpoint *LAG3* was overexpressed in acAE, predominantly in CD8+ cytotoxic T-cells (p-adj=2.1E-08, respectively) (**Figure 3O**). Intercellular communication analysis through CellChat (49) revealed a strong activity of LAG3 signaling in CD8+ cytotoxic T-cells in acAE (**Figure 3P**). *In vitro*, surface protein levels of CD25 and LAG3 significantly increased on T-cells upon stimulation with gp100-ImmTAC in a co-culture with gp100+ cells, validating the scRNA-seq findings (**Figure 3Q**).

Interestingly, *PDCD1* was not expressed in acAE (**Figure 3O**), but PD1 surface proteins were upregulated on T-cells *in vitro* upon stimulation with gp100-ImmTAC (**Figure 3Q**). However, significant

increases in PD1 were only observed at gp100-ImmTAC concentrations of 100 pM or 1000 pM on CD8+ and CD4+ T-cells, respectively; in contrast to LAG3, which was increased on CD8+ T-cells at 10 pM (**Figure 3Q**). To validate the dynamics of LAG3 and PD1 in UM, a published bulk RNA dataset of melanoma metastases from patients treated with tebentafusp was analyzed (3). Paired baseline and on-treatment tumor samples were available from two patients with UM. Both showed an increase in *LAG3* expression, while *LAG3* was decreased in 6 of 11 cutaneous melanoma (CM) patients (**Supplementary Figure 3F**). Conversely, *PDCD1* was not detected in both UM patients neither at baseline nor on-treatment, while it was expressed in 6 of 11 CM patients at both timepoints (**Supplementary Figure 3G**).

To assess the effectiveness of LAG3 inhibition in the context of tebentafusp treatment, CD8+ T-cells were co-cultured with target cells and treated with a combination of anti-LAG3 and anti-PD1 antibodies, as approved for CM (50), along with ImmTAC molecules (Supplementary Figure 3H). Significant activation of CD8+ T-cells (CD69 upregulation) was observed following anti-LAG3/PD1 blockade (Supplementary Figure 3H). These findings, together with the observed increase in LAG3 expression in skin-infiltrating CD8+ T-cells, suggest that LAG3/PD1 blockade - already established in clinical practice for CM (50) - may enhance ImmTAC-mediated T-cell redirection against target cells.

Melanocytes respond to IFN-γ, upregulate antigen presentation, and downregulate pigmentation genes

The melanocytes were of primary interest given their role as gp100 expressing cells in the normal skin. In the melanocytes of acAE samples, Antigen Processing and Presentation (e.g., *B2M, TAPBP, HLA-A, HLA-B, HLA-C, HLA-E*) as well as Response to IFN-γ (e.g., *CXCL10, IFI6, IFI27, IFITM3, PSME2*) Gene Ontology pathways were significantly overexpressed (**Figure 4A and B**). Simultaneously, genes involved in melanin pigment synthesis (e.g., *DCT, MITF*) showed significant downregulation (p-adj=2.5e-12, Cohen's *d* = 0.78) (**Figure 4C**).

Based on previous findings of IFN-γ-mediated downregulation of melanin synthesis (51), we hypothesized that tebentafusp-induced, immune cell-derived cytokines could be involved in the downregulation of melanin-associated genes. Indeed, decreased levels of DCT, a key enzyme in

melanin synthesis, were found in melanocytes treated with conditioned supernatant (derived from gp100-ImmTAC-redirected PBMC against gp100+ cells) *in vitro* (**Figure 4D**), which resulted in a visible reduction of melanin pigment (**Figure 4E**). DCT protein levels were rescued with an anti-IFN-γ, but not with an anti-IFN-β antibody, suggesting the observed downregulation in pigmentation depends on IFN-γ (**Supplementary Figure 4A**). Furthermore, *DCT* and *MITF* expression were negatively correlated with *CXCL10* in melanocytes (Pearson correlation -0.45 and -0.3, respectively) (**Figure 4F**). These findings indicate that tebentafusp-induced, T-cell-derived IFN-γ is involved in the activation of the melanocyte antigen presentation machinery and melanin synthesis inhibition.

PMEL (gp100) is not downregulated in response to tebentafusp

In the melanocytes, *PMEL* (gp100) expression was not reduced on tebentafusp treatment, in contrast to other pigmentation associated genes such as *DCT* and *MITF* (**Figure 4A and 4G)**. While both *DCT* and *PMEL* have previously been suggested to be regulated by *MITF* (52, 53), in our data only *DCT* but not *PMEL* expression was correlated with *MITF* (Pearson correlation 0.31 and 0.04, respectively) (**Figure 4H**). Furthermore, in contrast to *DCT* and *MITF*, *PMEL* expression did not negatively correlate with *CXCL10* (**Figure 4F and Supplementary Figure 4B**). However, the fraction of *PMEL*-expressing melanocytes showed a modest decrease from baseline to acAE of 7.0% (mean; range 1.5 to 15.9%) (**Supplementary Figure 4C**). These observations suggest *PMEL* expression to be more stable and less dependent on *MITF* and IFN-γ than other pigmentation genes.

Apoptotic signaling in melanocytes specifically increases in acAE

Next, we sought to explore melanocyte cell death as an explanation of the observed drop in melanocyte numbers (**Figure 2C**). There was a significant increase in the apoptosis-related gene expression signature in the melanocytes (**Figure 4I**), which was not detected in any other skin cell type (**Figure 4J**). Simultaneously, levels of anti-apoptotic genes such as *BCL-2, MCL1, BIRC-1* remained high (54) (**Figure 4K**). Indeed, quantification of apoptotic cells in acAE skin identified scattered cleaved caspase 3 positive cells, but with a significant increase compared to baseline skin ($p<0.01$) (**Figure 4L**).

Tebentafusp treatment induces a shift towards a pro-inflammatory macrophage state

Myeloid cells play key roles in cutaneous tissue repair and homeostasis (55). In the tumor microenvironment, they can assume pro- and anti-tumorigenic functions (56). Therefore, we aimed to elucidate their contribution to tebentafusp-mediated inflammation. Reclustering of myeloid cells resulted in 6 subclusters of macrophages and dendritic cells (DC) (**Figure 5A and B**). Macrophages separated into a pro-inflammatory M1-like (*IL1A, IL1B, IL6*) and an anti-inflammatory M2-like phenotype (*MRC1, CD163, F13A1*) (57) (**Figure 5B**). There was a significant increase in both the fraction of M1-like macrophages (p=0.004), and the ratio of M1:M2 from baseline to acAE (OR 2.88, 95% CI: 1.39 to 5.96, p=0.004) (**Figure 5C, Supplementary Figure 5A and B**).

Furthermore, macrophages significantly upregulated the pro-inflammatory genes *S100A8* and *S100A9* (avg.log2FC>3.29, p-adj<6.44e-13) (**Supplementary Figure 5C**). These are heterodimer-forming damage associated molecular pattern molecules (DAMP) known to be released from myeloid cells during inflammation and to induce cytokine secretion and leukocyte recruitment (58). Similarly, expression of the extracellular matrix component versican (*VCAN*) was increased, which is involved in regulation of immune cell trafficking and activation (avg.log2FC=1.85, p-adj=6.81e-08) (**Supplementary Figure 5C**) (59, 60). Together, these findings indicate a pro-inflammatory activation of macrophages in the skin on tebentafusp treatment.

Dendritic cells with immunoregulatory functions accumulate on tebentafusp treatment

The DCs clustered into mature DCs enriched in immunoregulatory molecules (mregDC; *LAMP3, BIRC3, CCR7*) (61, 62), plasmacytoid DC (pDC; *GZMB, IRF7, JCHAIN*) (63), classical DC type 1 (cDC1; *CLEC9A, IDO1, CADM1, DNASE1L3*) (57), and classical DC type 2 (cDC2; *CD1C, FCER1A, CLEC10A*) (57, 63) (**Figure 5B**).

The pDCs, which are specialized in type I interferon production, were only detected on treatment but not in baseline skin, consistent with previous observations of their recruitment to stressed skin (64) (**Figure 5C, Supplementary Figure 5A and B**).

The mregDC subcluster significantly increased in acAE ($p<0.005$) in all patients (**Figure 5C, Supplementary Figure 5A and B**). These are migratory DCs with immunoregulatory functions, as evidenced by high levels of both co-stimulatory genes such as *CD40*, *CD80* (B7-1), *TNFRSF9* (4-1BB) as well as immunosuppressive genes *CD274* (PD-L1), *IDO1*, *CD200* (**Figure 5B**) (65).

In summary, tebentafusp treatment caused cellular reorganization in the myeloid compartment. The recruitment of pDCs and mregDCs highlights the interplay of immuno-stimulatory and immuno-suppressive functions induced by tebentafusp.

Keratinocytes respond to tebentafusp treatment by upregulating pro-inflammatory genes

Besides barrier functions, keratinocytes can shape and amplify inflammatory signals in the skin (66). The keratinocytes subclustered into basal (*KRT5*), suprabasal (*KRT1*), cycling (*MKI67*), and hair follicle associated clusters (*FOXC1*) (67–69) (**Figure 5D and Supplementary Figure 5D**). There was no significant change in the subtype composition from baseline to acAE skin across all patients (**Supplementary Figure 5E, F and G**). IFN type I/II pathway responses and chemokine secretion were strongly upregulated (**Figure 5E**). Furthermore, the inflammatory intermediate filaments keratin 6 (*KRT6A, KRT6B, KRT6C*), 16 (*KRT16*) and 17 (*KRT17*), were upregulated, which are important regulators of epidermal innate immunity (**Figure 5E**) (70, 71). Several genes involved in epidermis development were downregulated, including *KRTDAP* (72), the transcription factor *MYC* (73), the nuclear hormone receptor *RORA* (74), components of intercellular desmosome junctions *DSP* and *PERP*, as well as the cell cycle inhibitors *CDKN1A* and *WEE1* (75) (**Figure 5E**).

Intercellular communication increases in acAE lesional skin

To explore changes in cell-cell communication induced by tebentafusp, receptor-ligand activity was inferred through CellChat analysis (49). The inferred overall interaction strength nearly doubled from baseline to acAE skin (**Supplementary Figure 5H**). Intercellular communication was affected very broadly in acAE as compared to baseline skin, with most cell types putatively interacting with each other (**Figure 5F**). On the receiving end, signaling to CD8+ T-cells and NK cells saw the largest increase (**Figure 5F and G**), largely by LAG3 signaling to CD8+ cytotoxic T-cells (**Figure 3P**).The strongest outgoing signal was observed in the melanocytes, followed by the proliferating T-cells and the myeloid cells (**Figure 5F and G**). In the melanocytes, fibronectin 1 (FN1) signaling and several HLA-molecules were predicted as the most active pathways (**Figure 5H**).

Melanocytes and keratinocytes secrete high levels of CXCL10 in lesional skin of tebentafusp treated patients

Transient systemic increases of the CXCL10 were reported as an acute response in patients treated with tebentafusp (3). Pharmacological modeling of cytokine dynamics following tebentafusp treatment predicted skin to be the major contributor of CXCL10 release (76). Interestingly, in our scRNA-seq analysis, we identified melanocytes and keratinocytes as the cell types with the largest overexpression of *CXCL10* upon tebentafusp treatment (**Figure 5I**). Tebentafusp-mediated CXCL10 secretion was validated *in vitro* at the protein level in a gp100-dependent fashion (**Figure 5J**), suggesting that melanocytes and keratinocytes likely contribute to the transient systemic cytokine increase.

Discussion

We analyzed 11 UM patients treated with tebentafusp, 81% of whom developed an acAE within hours of infusion. The appearance of early-onset acAE is in line with previous findings that reported incidences of more than 80% at any grade within the first 3-4 weekly infusions (1, 12). Most reactions were transient erythema, with one case each of maculopapular and bullous lesions, similar to prior reports (17). Later in treatment, 63.6% developed a VLPD of skin or hair, a higher incidence than the previously reported 45–57% (13, 16), This may be due to increased treatment beyond progression in real-world settings or the small cohort size.

The majority of patients developed acAE within 12 to 48 hours after the first three weekly infusions. This rapid onset contrasts with the delayed cAE seen with ICI like anti-CTLA4/PD1/PDL1 (77). Unlike ICIs, which inhibit immunosuppressive molecules on T-cells in the skin, tebentafusp directly recruits and activates T-cells toward target antigen-expressing cells, triggering an immediate polyclonal T-cell response. This likely explains the rapid T-cell migration into the skin and the early onset of acAE. The transient nature of acAE aligns with the short half-life of tebentafusp and the observed cytokine peak within 24 hours post-dose (3), distinguishing them from ICI-induced cAE, which can persist even after treatment discontinuation. These observations suggest that the acAE reflect tebentafusp's pharmacodynamics and pharmacokinetics in an on-target, off-tumor fashion.

Phase I/II and III trials found a correlation of acAE occurrence with longer OS, which we confirm in our small real-world analysis (1, 3). However, this association was dependent on other known prognostic factors such as LDH levels, ECOG performance score and metastatic burden (14). Therefore, acAE likely reflect overall immune fitness and responsiveness to tebentafusp, rather than serving as an independent predictor of outcome. These findings support the notion that acAE mirror the tebentafusp's pharmacodynamics.

Histological analyses of skin reactions to tebentafusp revealed CD4+ and CD8+ T-cells infiltration with a high density close to melanocytes, resembling a lichenoid reaction pattern. Similarly, T-cell numbers increase in tumor tissue on treatment (3). ScRNAseq analysis showed proliferation and high metabolic

activity of CD4+ and CD8+ T-cells in acAE, indicating polyclonal T-cell recruitment and activation, consistent with previous findings (9). The preferential enrichment and retainment of CD8+ T-cells near melanocytes suggests their potentially contributing to tebentafusp-induced depigmentation. CellChat, a tool for analyzing cellular communication via scRNA-seq, models signaling dynamics through ligand-receptor interactions (49) and can determine interaction strength, directionality and cell type specific communication changes. CellChat predicted an increase in signal reception within CTLs, while melanocytes showed the highest increase in outgoing signaling, further supporting a tebentafusp-driven interaction between these two populations.

We observed Treg activation in tebentafusp-induced acAE via *IL2RA* upregulation, a common feature of bispecific T-cell engagers (44). This suggests that combining tebentafusp with Treg-targeted therapies or IL-2 variants that preferentially expand effector over regulatory T-cells (78), may boost efficacy, though possibly at the cost of tolerability.

In the myeloid compartment, macrophages shifted to a pro-inflammatory M1-like phenotype likely due to the activation of skin-resident macrophages, as mIHC showed no significant increase in overall macrophage numbers. Overall macrophage levels remained unchanged, differing from other studies (14). However, mregDC levels increased significantly in acAE. These immunoregulatory DCs are normally rare in skin (62), but quickly infiltrate inflamed sites (79). MregDC exhibit both co-stimulatory (CD80) and immunosuppressive functions (PD-L1) (65) and their PD-L1 expression parallels its increase in tumors treated with tebentafusp, mostly driven by IFN-γ responses (3, 80, 81). Therefore, mregDC may contribute to immunoregulatory signaling, though their role in tebentafusp activity remains unclear and warrants further investigation.

In patients treated with tebentafusp, CXCL10 showed the highest serum increase, peaking within 24 hours post-dose (82). This CXCL10 surge correlated with extravasation of CXCR3+ CD8+ T-cells, leading to greater tumor shrinkage and improved survival (3, 82). In our study melanocytes showed the greatest *CXCL10* increase among skin cells along with strong upregulation of IFN-γ response genes. This aligns with a pharmacodynamic model predicting that skin-resident immune cells are a major source of systemic cytokines (76). Furthermore, it suggests that melanocytes and keratinocytes

contribute to cytokine release syndrome (CRS), warranting further research into CXCL10 and IFN-γ as potential CRS biomarkers or therapeutic targets.

Tebentafusp-induced T-cell cytotoxicity and IFN-γ release triggered apoptotic signaling in melanocytes, resembling mechanisms seen in vitiligo (51). A study from Gallatly *et al.,* identified cytotoxic CD8+ T-cells as key mediators of melanocyte destruction and highlighted the CCL5-CCR5 axis in regulating CD8+ T-cell and Treg interactions within the skin (83). Dysregulation of this pathway contributes to vitiligo progression, while IFN-γ amplifies inflammation, further driving melanocyte loss and pigment suppression. Similar to tebentafusp-induced changes, *CXCL10* and *IFNG* were highly expressed in keratinocytes and T-cell populations, respectively (83). However, these conditions arise in distinct contexts: vitiligo is a chronic autoimmune disorder, while tebentafusp-induced skin inflammation is an acute, drug-induced response caused by on-target, off-tumor T-cell activation. Notably, it was shown that patients who developed vitiligo under tebentafusp had higher survival rates, suggesting a potential link between off-tumor and on-tumor immune mechanisms (16).

While early on tebentafusp treatment there is a strong increase in CD8+ T-cells, in the VLPD lesions, they were increased in only two patients. This is likely because biopsies were taken from the center of the lesion, a region characterized by lower disease activity than the borders, where depigmentation has already occurred and the T-cells have left.

In our tebentafusp-treated cohort, melanocytes were significantly reduced in acAE skin. While in vitro studies suggested lower gp100 levels in normal melanocytes limit direct tebentafusp-induced killing (42) cleaved caspase 3 staining indicated low apoptosis rates (84). This resistance may be due to high BCL-2 expression (54).

Intercellular communication analysis revealed a strong increase in paracrine signaling, especially between melanocytes, myeloid cells, and CD8+ T-cells. Melanocytes upregulated FN1, an extracellular vesicle protein with anti-apoptotic functions, linked to a mesenchymal melanoma phenotype and poor prognosis in CM and UM (85). Therefore, FN1's role in tebentafusp resistance warrants further study.

Melanocytes in acAE downregulated pigmentation genes, consistent with in vitro findings (8). Pigmentation loss correlated with CXCL10 expression, suggesting inflammation-driven pigment inhibition combined with scattered melanocyte death as the cause of VLPD. Gp100 (*PMEL*) expression remained stable, independent of MITF or IFN-γ regulation. Immunohistochemistry showed no gp100 loss in melanoma metastases, and previously reported PMEL decreases were likely due to melanocyte loss rather than transcriptional downregulation (14). A 7% increase in PMEL-negative melanocytes in acAE suggests preferential killing of PMEL-expressing melanocytes.

In acAE, melanocytes upregulated antigen-presenting machinery genes, mirroring changes seen in tumor samples (3, 86). This machinery may have dual roles in tebentafusp treatment: it correlates with improved survival by increasing gp100-pHLA surface presentation, enhancing T-cell activation (87, 88), but can also inhibit immune responses through HLA-A/B/C and HLA-E signaling to NK cell receptors (89) or HLA class II interactions with LAG3 (90). LAG3 expression was upregulated in acAE and UM metastases (n=2) post-tebentafusp, whereas PD1 showed variable expression, increasing in vitro at higher gp100-ImmTAC concentrations but not in skin or metastases, likely due to the use of healthy donor T-cells in vitro. CellChat analysis and co-culture assays confirmed LAG3 signaling in cytotoxic T-cells, aligning with prior findings that LAG3, rather than PD1, drives T-cell exhaustion in UM (91, 92). Similar findings were reported with blinatumomab, another bispecific T-cell engager, where LAG3 was upregulated but not PD1 (44). These results suggest that LAG3-targeted therapies could enhance tebentafusp efficacy, though potentially at the cost of increased toxicity.

We hypothesize that the on-target, off-tumor mechanisms observed in skin biopsies from tebentafusp-treated patients may provide valuable insights into its mechanism of action in the tumor microenvironment. However, intratumoral dynamics during treatment remains poorly understood due to the challenges of repeated liver metastasis sampling. For this reason, a direct comparison of matched skin and metastasis samples was not covered, representing a key limitation of our study.

In summary, we provide comprehensive insights into the single-cell dynamics associated with the on-target, off-tumor effects in skin inflammation in response to tebentafusp. Our key results of melanocytes and keratinocytes' role in feed-forward loop of cutaneous and systemic inflammatory processes, as

492 well as the upregulation of LAG3 after treatment initiation, warrant a deeper investigation if these
493 pharmacodynamics reflect the events that occur in the tumor microenvironment and possible
494 therapeutic opportunities. Identifying shared or distinct targets that contribute to treatment escape or
495 toxicity may lead to improved efficacy and tolerability of bispecific T-cell engagers.

Material and Methods

Sex as a biological variable

The patient cohort included both male and female patients, as detailed in **Supplementary Table 1**.

Clinical information and survival analysis

We included consenting patients with mUM receiving tebentafusp (Kimmtrak®) in an expanded access program at the University Hospital Zurich, Switzerland (NCT04960891). Clinical information and experimental details are summarized in **Supplementary Table 1, 2 and 3**. Adverse events were graded according to Common Terminology Criteria for Adverse Events (CTCAE) v5. For survival analysis, R packages survival v3.5 and survminer v0.4.9 were used.

LDH measurements

LDH was measured in the patients' serum using the International Federation of Clinical Chemistry (IFCC) method by Roche.

Human primary tissue and live slow-frozen biobanking

Skin biopsies were collected from consenting patients and stored in the Dermatology Biobank as live slow-frozen samples for scRNA-seq as previously described (19) and formalin-fixed paraffin-embedded (FFPE) samples for histology and immunohistochemistry (**Supplementary Table 1**). Histology and immunohistochemistry: FFPE skin samples were stained with hematoxylin and eosin (H&E) for standard histology or using the following antibodies for immunohistochemistry: anti-CD3 (Roche, 2GV6), anti-MelanA (Roche, A103), anti-SOX10 (Cell Marque, EP268), anti-Tyrosinase (Roche, T311). Immunohistochemistry staining was performed on a Ventana BenchMark Ultra (Roche) with the UltraView Universal Alkaline Phosphatase Red Detection Kit. TUNEL and cleaved caspase 3 stainings were performed by Sophistolab, Switzerland.

H&E histologies were assessed by an experienced dermatopathologist based on qualitative grading (grade 0=absent, 1=weak, 2=moderate, 3=strong). Image analysis of TUNEL and cleaved caspase 3

stainings was performed in QuPath software V0.3.0. Automatic estimation of stain vectors was performed using a representative area. To assess epidermal cell death via TUNEL staining, the epidermis was selected and positive cell detection was run using preset parameters and a single threshold for mean nuclear staining intensity. From the same images, epidermal cell sizes were exported. For statistical analysis of TUNEL staining and epidermal cell sizes, a generalized linear mixed-effects model was fit using the *lmer()* function from the lme4 package in R, expressing the positive fraction of cells or the cell size, respectively, as a function of time point, with patient identity as a random variable and the model was fit using a binomial link function. For analysis of apoptotic cells via cleaved caspase 3 staining, the basal layer was selected and positive cell detection was run using preset parameters and a single threshold for mean cellular staining intensity.

Multiplex Immunohistochemistry

For mIHC, the Opal technology was used (Akoya Biosciences, NEL871001KT). Following primary antibodies were used: anti-CD8 (ABCAM ab4055), anti-CD68 (ABCAM ab213363), anti-MelanA (NovusBiologicals NBP1-30151), anti-CD4 (LeicaBiosystems, 4B12), anti-Sox10 (ABCAM ab268113), anti-PanCK (SantaCruz, sc-8018). Staining was performed on a Bond RXm (LeicaBiosystems) following manufacturer instructions. Scanning was performed on a PhenoImager HT (Akoya Biosciences).

Spectral unmixing and cell segmentation was performed with inForm 2.4.9 software. Cell segmentation data was imported to R using the Giotto package v2.0.0.998 . Cell identities of CD4+ T-cells, CD8+ T-cells, CD68+ macrophages, PanCK+ keratinocytes, and SOX10+ MelanA+ melanocytes based on leiden clustering. One unannotated cluster negative for these six markers was labeled as “Other”. Cell percentages were calculated for each patient separated by condition. Percentages were then transformed to centered log ratios using the clr() function from the R package compositions v2.0-6, enabling the compositional data to be analyzed independently of the dependencies between the components. Significance was calculated using the t_test() function from R package rstatix using an FDR correction to obtain adjusted p-values.

Spatial location data obtained from inForm 2.4.9 software was utilized to plot cell locations to create a visualization of the patient biopsies in two dimensional space. From the phenoptr package v0.3.2 (93),

the function count_within() was used to calculate the average number of each immune cell type within a specified radius of the melanocytes. Ten radii from 10 to 100 µm were used in 10 µm increments. Areas for each donut were calculated by subtracting the previous increment's area, forming rings except for the initial 10 µm circle. The average number of immune cells in each space was divided by their areas to determine cell density.

Enzymatic dissociation of live slow-frozen skin biopsies for scRNA-seq

Enzymatic dissociation of live slow-frozen skin biopsies for scRNA-seq was performed using two step digestion as previously described (94). Cell count and viability was accessed on Luna-FL™ cell counter (LogosBiosystems, cat.no.L1001) using AOPI live/dead staining (LogosBiosystems, cat.no.F23001) with counting slides (LogosBiosystems, cat.no.L12005) and optimal cell concentration was adjusted according to 10XGenomics recommendation (700-1200 cells/µl).

Single-cell processing was performed using a 10XGenomics Chromium Single-Cell Controller following the manufacturer guidelines. Paired-end sequencing (PE 28/8/0/91) was performed on the Illumina NovaSeq SP flow cell. According to 10XGenomics recommendation, with >20,000 read pairs per cell for GEX.

Data Analysis of scRNA-seq results

Raw reads were demultiplexed and aligned against the human reference genome assembly GRCh38.p13 using the 10x Genomics CellRanger v6.0.2 pipeline. The R package Seurat v4.1.1 was used for the downstream analyses of the filtered count matrices. Cells with unique feature counts <250 or >4,000-6,000, unique UMI counts >20,000, mitochondrial gene counts >15-30% and ribosomal gene counts >40% were discarded as part of quality control. Filtered samples were log normalized and integrated using canonical correlation analysis. Integrated data was scaled and principal component analysis was performed using the top 2000 variable features for dimensional reduction. Samples were clustered together using Louvain-algorithm with a resolution of 0.4 based on top 30 principal components (PCs). For each cell cluster, Wilcoxon rank-sum test was applied to identify the marker genes with log2 fold change > 0.25 and adjusted p-value < 0.01 cut-offs. Cell clusters were annotated

based on known markers from literature (19, 69, 95). For specific cell types, cells were re-clustered using top 18 PCs and cluster resolution of 0.6 following the same steps as mentioned above.

Differential abundance analysis was performed for T and myeloid cell subcluster compositions. Exact test from the R package edgeR v4.0 was applied to measure the cell subcluster proportion differences between the two conditions.

Differential gene expression analysis (likelihood ratio test with patient effect as latent variable) was performed with FindMarkers() function from the Seurat package. Differential genes with log2 fold-change >0.5 and adjusted p-value <0.05 cut-offs were considered to be significant. GeneOntology pathway (GO BP) enrichment analysis was performed with the R package SCpubr v2.0.1 (96).

Gene expression signature scores were computed with AddModuleScore() function from the Seurat package. Wilcoxon rank-sum test was used as a statistical test and effect size was calculated as Cohen's *d* using the effectsize package. Following signatures were used:

- Gylcolysis: *ENO1*, *GAPDH*, *PGK1*, *PKM*, and *LDHA* (97)
- Cytotoxicity: *GZMA*, *GZMB*, PRF1, *NKG7* (98)
- IFN-γ signaling: MSigDB hallmark gene set (99)
- Pigmentation: GeneOntology GO:0043473 (100)
- Apoptosis: Kyoto Encyclopedia of Genes and Genomes (KEGG) hsa04210, 87 genes (101)

Cell-cell interaction analysis was performed using the R package CellChat (49). The ligand-receptor database CellChatDB was updated with LAG3 receptor-ligand interactions (102). Only T-cells, myeloid cells, keratinocytes and melanocytes were considered for the CellChat analysis.

The R packages SCpubr v2.0.1 and Seurat v4.1.1 packages were used for visualization of scRNA-seq results (96).

Tumor expression data

From a published Nanostring tumor gene expression dataset of melanoma patients treated with tebentafusp (3), data for *LAG3* and *PDCD1*, which had not been reported on in that publication, was made accessible upon request. Results for 13 patients with a paired baseline and on-treatment sample (within 3 weeks post tebentafusp infusion) and information on melanoma subtype (2 uveal, 11 non-uveal) were available. The raw data was log2-normalized.

In vitro assays

PBMC and T-cell isolation: 100-200 ml blood was obtained from healthy donors and peripheral blood mononuclear cells (PBMC) were isolated by density gradient centrifugation over Lymphoprep (Axis-Shields, UK). Negative T-cells enrichment was performed using Pan T-Cell Isolation Kit (Miltenyi, Germany) following manufacturer's instructions.

Measurement of T-cell activation and proliferation in response to ImmTAC-redirection: MEL624 (obtained from NCI), an HLA-A*02:01+ gp100+ CM cell line was used in ImmTAC redirection assays. T-cell proliferation assay: Pan T-cells were pre-stained with 2.5 µM CellTrace Violet (CTV, ThermoFisher, UK) according to the manufacturer's guidelines. Tumour cells were co-cultured with Pan T-cells (5:1 Effector: Target ratio) in the presence or absence of gp100-ImmTAC concentrations of (10, 100, 1000 pM) for 5 days. T-cell activation was measured after 24 and 48h of redirection by flow cytometry. T-cell proliferation was assessed at the end of the assay. Cells were harvested and stained with Zombie-NIR (Biolegend, UK) to assess viability and fluorochrome-conjugated antibodies against CD3-APC (UCHT1), CD4-PE Cy7 (RPA-T4), CD8-BV650 (SK1), PD1-PE (NAT105), LAG3-BV785 (11C3C65; all from Biolegend, UK), and CD25-BUV395 (2A3, BD Biosciences, UK). Cells were fixed with BD Stabilizing Fixative (BD Biosciences, UK). Samples were acquired on a BD LSRFortessaTM X-20 flow cytometer. Phenotypic markers of live CD4 and CD8 T-cells were analysed using FlowJo V10.5.3 (TreeStar, USA). T-cell proliferation analysis (Expansion index and precursor frequency) was determined based on CTV staining as previously described in (103). To assess the influence of LAG-3 and PD-1 checkpoint blockade, T-cells and tumor co-culture assays in the presence of ImmTAC molecules were repeated in the presence or absence of anti-LAG3 (10 µg/ml, 11E3, Abcam, UK) and anti-PD-1 (Pembrolizumab) Ab (10 µg/ml, Selleck Biotechnology Ltd, UK). Cells were then stained with antibodies against CD4 BUV496 (SK3), CD8 BUV805 (SK1; both from BD Biosciences), CD69 BV711 (FN50), CD3 PE-Fire810 (17A2; both from Biolegend, UK) and analyzed by flow cytometry as described above.

Measurement of cytokine and chemokine production: T2 cells (ATCC, USA) were pulsed with increasing concentrations of gp100 peptide (YLEPGPVTV) for 2 hours at 37 °C. Cells were washed and co-cultured with Pan T-cells at 1:5, 1:1, or 5:1 E:T ratios, in the presence or absence of 10-100 pM

tebentafusp (Immunocore Ltd, UK). Cytokines and chemokines within culture supernatants collected at 24h or 48h were measured by electrochemiluminescence using a combination of MSD U-plex and R-plex kits (MesoScaleDiscovery, USA). The assays were performed in duplicate following the manufacturer's protocols and analysed using MSD QuickPlex SQ120 Reader (MesoScaleDiscovery, USA). Data analysis was performed using MSD Discovery Workbench 4.0.12 software (MesoScaleDiscovery, USA).

Melanin synthesis analysis: Normal Human Epidermal Melanocytes (NHEM) were used to assess the effects of tebentafusp-induced inflammation on the melanin synthesis pathway. NHEM4 (PromoCell, Germany), NHEM9 (ATCC, USA), and NHEM10 (Lonza, Switzerland) were cultured according to the suppliers' instructions and recommended media. Supernatants from tebentafusp-redirected PBMC against melanoma cells (MEL526, obtained from NCI) were collected and transferred onto NHEM cells. Cells were cultured for 72h in the presence or absence of 10 µg/ml neutralizing antibodies against IFNγ (B27), or IFNβ (IFNb/A1; both from Biolegend, UK). Cells were harvested and their melanin content was quantified by absorbance at 405nm using a Clariostar spectrophotometer (BMG Labtech, Germany) as previously described in (104). A standard curve was generated using synthetic melanin (Sigma-Aldrich, UK) dissolved in 1 N NaOH (0-500 µg/mL). NHEM cell pellets were lysed with RIPA buffer (ThermoFisher, UK) containing protease inhibitors (Sigma Aldrich, UK) followed by boiling at 95^{o}C. Protein were quantified using the Pierce BCA protein assay kit (ThermoFisher, UK) and loaded onto Bolt 4-12% Bis-Tris plus gels (ThermoFisher, UK). Melanin synthesis proteins were quantified by western blot (WB) using antibodies against human GAPDH (6C5, Millipore), Tyrosinase (ab180753), TRP1 (ab3312), TRP2/DCT (ab180753), and MITF (ab12039; all from Abcam, UK) and goat anti-rabbit IgG and goat anti-mouse IgG secondary antibodies (CellSignaling, USA). WB were performed using the Li-COR system and membranes were scanned on the LI-COR C-DiGit Blot Scanner (LI-COR, USA).

IFN-γ and GZMB ELISpot assays: The melanoma cell lines Mel526 (HLA-A*0201 positive and gp100 positive) and A375 (HLA-A*0201 positive and gp100 negative; both obtained from ATCC) were used as positive and negative controls respectively, and were maintained in RPMI supplemented with 2 mM L-glutamine, 10 % FCS, 50 units/mL penicillin and 50 ug/mL streptomycin. The number of PBMCs added per well varied according to which PBMC preparation which had been previously titrated on

Mel526 cells in order to determine the number of effector cells required per well. Reactivity between donor PBMC and NHEM melanocytes in the presence of varying IMCgp100 concentrations was assessed by IFN-γ and GZMB ELISpot following manufacturer's protocol (BD Biosciences).

Statistics summary

P values <0.05 were considered significant. Student's t-tests were 2-tailed, ANOVA were 2-way.

Ethics declarations

The collection and use of clinical material for research purposes was approved by the Cantonal Ethics Committee Zurich (BASEC PB.2018-00194, KEK2019-02150) and patient informed consent was obtained for all human primary material.

Data availability

Supporting data values are provided in the corresponding file. The scRNA-seq data is available from GEO, accession number GSE259383.

Acknowledgements

We thank SKINTEGRITY.CH and Functional Genomics Center Zurich of University of Zurich and ETH Zurich for their support.

Author contributions

Conceptualization: RS, AT, ER, MPL, RD, and BMS. Data collection: RS, AT, NW, IK, ABe, JH, ABr, AC, and BMS. Data analysis: RS, AT, AG, PS, PT, VH, PC, SK, BB, and BMS. Visualization: RS, AT, and AG. Resources: MPL, RD, and BMS. Writing - original draft: RS, AT, AG, and BMS. Reviewing and editing: IK, ABe, VH, ER, JPP, SK, BB, MPL, RD, and BMS.

Declaration of interests

ABe, ABr, JH, and AC are current or former employees of Immunocore. ER has intermittent, project-focused consulting and/or advisory relationships or has received travel or research grants from Sanofi, Pierre Fabre, Bristol-Myers Squibb (BMS), Amgen, Galderma, Takeda, SunPharma, Novartis, Merck Sharp&Dhome (MSD), and Leo-Pharma outside the submitted work. LK has intermittent consultant relationships with Johnson&Johnson outside the submitted work. RD has intermittent, project-focused consulting and/or advisory relationships or has received travel or research grants from Novartis, MSD, BMS, Roche, Amgen, Takeda, Pierre Fabre, SunPharma, Sanofi, Catalym, Second Genome, Regeneron, Alligator, T3 Pharma, MaxiVAX SA, Pfizer, Simcere, and touchIME outside the submitted work. MPL received funding in the past for unrelated research projects from Oncobit, Roche, Novartis, Molecular Partners, and Scailyte BMS has intermittent, project-focused consulting, advisory relationships or has received travel or research grants from Johnson&Johnson, Abbvie, Roche and Incyte. The remaining authors declare no competing interests.

References

1. Nathan P, et al. Overall Survival Benefit with Tebentafusp in Metastatic Uveal Melanoma. *N Engl J Med*. 2021;385(13):1196–1206.

2. Oates J, Hassan NJ, Jakobsen BK. ImmTACs for targeted cancer therapy: Why, what, how, and which. *Mol Immunol*. 2015;67(2 Pt A):67–74.

3. Middleton MR, et al. Tebentafusp, A TCR/Anti-CD3 Bispecific Fusion Protein Targeting gp100, Potently Activated Antitumor Immune Responses in Patients with Metastatic Melanoma. *Clin Cancer Res*. 2020;26(22):5869–5878.

4. Lowe KL, et al. Novel TCR-based biologics: mobilising T cells to warm “cold” tumours. *Cancer Treat Rev*. 2019;77:35–43.

5. Cole D, et al. Abstract 2271: Tebentafusp recognition of melanoma cells is restricted by HLA-A0201 presentation of a gp100 peptide. *Cancer Research*. 2020;80 (16_Supplement): 2271. https://doi.org/10.1158/1538-7445.am2020-2271.

6. Hurley CK, et al. Common, intermediate and well-documented HLA alleles in world populations: CIWD version 3.0.0. *Hladnikia* . 2020;95(6):516–531.

7. Hoashi T, et al. The Repeat Domain of the Melanosomal Matrix Protein PMEL17/GP100 Is Required for the Formation of Organellar Fibers*. *J Biol Chem*. 2006;281(30):21198–21208.

8. Vardeu M, et al. 624 IFNγ secreted by tebentafusp (IMCgp100)-redirected T cells inhibits expression of melanin synthesis pathway genes in healthy melanocytes. *J Immunother Cancer*. 2020;8(Suppl 3). https://doi.org/10.1136/jitc-2020-SITC2020.0624.

9. Boudousquie C, et al. Polyfunctional response by ImmTAC (IMCgp100) redirected CD8+ and CD4+ T cells. *Immunology*. 2017;152(3):425–438.

10. Jager MJ, et al. Uveal melanoma. *Nat Rev Dis Primers*. 2020;6(1):24.

11. Yang J, et al. Treatment of uveal melanoma: where are we now? *Ther Adv Med Oncol*. 2018;10:1758834018757175.

12. Hassel JC, et al. Three-Year Overall Survival with Tebentafusp in Metastatic Uveal Melanoma. *N Engl J Med*. [published online ahead of print: October 21, 2023]. https://doi.org/10.1056/NEJMoa2304753.

13. Hassel JC, et al. Co-primary endpoint of overall survival for tebentafusp (tebe)-induced rash in a phase 3 randomized trial comparing tebe versus investigator's choice (IC) in first-line metastatic uveal melanoma. *J Clin Oncol*. 2021;39(15_suppl):9527–9527.

14. Hassel JC, et al. Tebentafusp induces a T cell driven rash in melanocyte-bearing skin as an adverse event consistent with the mechanism of action. *J Invest Dermatol*. 2024;(24):1886–1890.

15. Hassel JC, et al. Practical guidelines for the management of adverse events of the T cell engager bispecific tebentafusp. *Eur J Cancer*. 2023;191:112986.

16. Orloff M, et al. Abstract 3295: Vitiligo and other clinical melanocyte-related adverse events following tebentafusp (IMCgp100) exposure in patients with uveal melanoma [preprint]. *Immunology*. 2020. https://doi.org/10.1158/1538-7445.am2020-3295.

17. Pham JP, et al. A review of the cutaneous toxicities of tebentafusp-Featuring two cases involving superficial bullous reactions. *Australas J Dermatol*. [published online ahead of print: May 5, 2022]. https://doi.org/10.1111/ajd.13866.

18. Grasl-Kraupp B, et al. In situ detection of fragmented DNA (TUNEL assay) fails to discriminate among apoptosis, necrosis, and autolytic cell death: a cautionary note. *Hepatology*. 1995;21(5):1465–1468.

19. Restivo G, et al. Live slow-frozen human tumor tissues viable for 2D, 3D, ex vivo cultures

741 and single-cell RNAseq. *Commun Biol*. 2022;5(1):1144.

742 20. Campbell JJ, et al. The chemokine receptor CCR4 in vascular recognition by cutaneous
743 but not intestinal memory T cells. *Nature*. 1999;400(6746):776–780.

744 21. Andrew DP, et al. C-C chemokine receptor 4 expression defines a major subset of
745 circulating nonintestinal memory T cells of both Th1 and Th2 potential. *J Immunol*.
746 2001;166(1):103–111.

747 22. Liao F, et al. CC-chemokine receptor 6 is expressed on diverse memory subsets of T
748 cells and determines responsiveness to macrophage inflammatory protein 3 alpha. *J*
749 *Immunol*. 1999;162(1):186–194.

750 23. de Almeida GP, et al. Human skin-resident host T cells can persist long term after
751 allogeneic stem cell transplantation and maintain recirculation potential. *Sci Immunol*.
752 2022;7(67):eabe2634.

753 24. Szabo PA, et al. Single-cell transcriptomics of human T cells reveals tissue and
754 activation signatures in health and disease. *Nat Commun*. 2019;10(1):4706.

755 25. Tan JT, et al. IL-7 is critical for homeostatic proliferation and survival of naive T cells.
756 *Proc Natl Acad Sci U S A*. 2001;98(15):8732–8737.

757 26. Kondrack RM, et al. Interleukin 7 regulates the survival and generation of memory CD4
758 cells. *J Exp Med*. 2003;198(12):1797–1806.

759 27. Azizi E, et al. Single-Cell Map of Diverse Immune Phenotypes in the Breast Tumor
760 Microenvironment. *Cell*. 2018;174(5):1293–1308.e36.

761 28. Clarke J, et al. Single-cell transcriptomic analysis of tissue-resident memory T cells in
762 human lung cancer. *J Exp Med*. 2019;216(9):2128–2149.

763 29. Mackay LK, et al. The developmental pathway for CD103(+)CD8+ tissue-resident

764 memory T cells of skin. *Nat Immunol*. 2013;14(12):1294–1301.

765 30. Boddupalli CS, et al. ABC transporters and NR4A1 identify a quiescent subset of tissue-
766 resident memory T cells. *J Clin Invest*. 2016;126(10):3905–3916.

767 31. Crowl JT, et al. Tissue-resident memory CD8+ T cells possess unique transcriptional,
768 epigenetic and functional adaptations to different tissue environments. *Nat Immunol*.
769 2022;23(7):1121–1131.

770 32. Milner JJ, et al. Runx3 programs CD8+ T cell residency in non-lymphoid tissues and
771 tumours. *Nature*. 2017;552(7684):253–257.

772 33. Skon CN, et al. Transcriptional downregulation of S1pr1 is required for the establishment
773 of resident memory CD8+ T cells. *Nat Immunol*. 2013;14(12):1285–1293.

774 34. Debes GF, et al. Chemokine receptor CCR7 required for T lymphocyte exit from
775 peripheral tissues. *Nat Immunol*. 2005;6(9):889–894.

776 35. Zemmour D, et al. Single-cell gene expression reveals a landscape of regulatory T cell
777 phenotypes shaped by the TCR. *Nat Immunol*. 2018;19(3):291–301.

778 36. Böttcher JP, et al. NK Cells Stimulate Recruitment of cDC1 into the Tumor
779 Microenvironment Promoting Cancer Immune Control. *Cell*. 2018;172(5):1022–1037.e14.

780 37. Ng SS, et al. The NK cell granule protein NKG7 regulates cytotoxic granule exocytosis
781 and inflammation. *Nat Immunol*. 2020;21(10):1205–1218.

782 38. Goda C, et al. Involvement of IL-32 in activation-induced cell death in T cells. *Int*
783 *Immunol*. 2006;18(2):233–240.

784 39. Cano-Gamez E, et al. Single-cell transcriptomics identifies an effectorness gradient
785 shaping the response of CD4+ T cells to cytokines. *Nat Commun*. 2020;11(1):1801.

786 40. Wagner SN, et al. Analysis of Pmel17/gp100 expression in primary human tissue

787 specimens: implications for melanoma immuno- and gene-therapy. *Cancer Immunol*
788 *Immunother*. 1997;44(4):239–247.

789 41. Liddy N, et al. Monoclonal TCR-redirected tumor cell killing. *Nat Med*. 2012;18(6):980–
790 987.

791 42. Harper J, et al. An approved in vitro approach to preclinical safety and efficacy
792 evaluation of engineered T cell receptor anti-CD3 bispecific (ImmTAC) molecules. *PLoS*
793 *One*. 2018;13(10):e0205491.

794 43. Menk AV, et al. Early TCR Signaling Induces Rapid Aerobic Glycolysis Enabling Distinct
795 Acute T Cell Effector Functions. *Cell Rep*. 2018;22(6):1509–1521.

796 44. Huo Y, et al. Blinatumomab-induced T cell activation at single cell transcriptome
797 resolution. *BMC Genomics*. 2021;22(1):1–16.

798 45. Franchimont D, et al. Positive effects of glucocorticoids on T cell function by up-
799 regulation of IL-7 receptor alpha. *J Immunol*. 2002;168(5):2212–2218.

800 46. Schluns KS, et al. Interleukin-7 mediates the homeostasis of naïve and memory CD8 T
801 cells in vivo. *Nat Immunol*. 2000;1(5):426–432.

802 47. Ladányi A, et al. T-cell activation marker expression on tumor-infiltrating lymphocytes as
803 prognostic factor in cutaneous malignant melanoma. *Clin Cancer Res*. 2004;10(2):521–530.

804 48. Solomon I, et al. CD25-Treg-depleting antibodies preserving IL-2 signaling on effector T
805 cells enhance effector activation and antitumor immunity. *Nat Cancer*. 2020;1(12):1153–
806 1166.

807 49. Jin S, et al. Inference and analysis of cell-cell communication using CellChat. *Nat*
808 *Commun*. 2021;12(1):1088.

809 50. Tawbi HA, et al. Relatlimab and nivolumab versus nivolumab in untreated advanced

melanoma. *N Engl J Med*. 2022;386(1):24–34.

51. Yang L, et al. Interferon-gamma Inhibits Melanogenesis and Induces Apoptosis in Melanocytes: A Pivotal Role of CD8+ Cytotoxic T Lymphocytes in Vitiligo. *Acta Derm Venereol*. 2015;95(6):664–670.

52. Bertolotto C, et al. Different cis-acting elements are involved in the regulation of TRP1 and TRP2 promoter activities by cyclic AMP: pivotal role of M boxes (GTCATGTGCT) and of microphthalmia. *Mol Cell Biol*. 1998;18(2):694–702.

53. Du J, et al. MLANA/MART1 and SILV/PMEL17/GP100 are transcriptionally regulated by MITF in melanocytes and melanoma. *Am J Pathol*. 2003;163(1):333–343.

54. McGill GG, et al. Bcl2 regulation by the melanocyte master regulator Mitf modulates lineage survival and melanoma cell viability. *Cell*. 2002;109(6):707–718.

55. Joshi N, et al. Comprehensive characterization of myeloid cells during wound healing in healthy and healing-impaired diabetic mice. *Eur J Immunol*. 2020;50(9):1335–1349.

56. Park MD, et al. On the Biology and Therapeutic Modulation of Macrophages and Dendritic Cells in Cancer. *Annu Rev Cancer Biol*. 2023;7(1):291–311.

57. Xue D, et al. Transcriptome landscape of myeloid cells in human skin reveals diversity, rare populations and putative DC progenitors. *J Dermatol Sci*. 2020;97(1):41–49.

58. Wang S, et al. S100A8/A9 in Inflammation. *Front Immunol*. 2018;9:1298.

59. Wight TN, Kang I, Merrilees MJ. Versican and the control of inflammation. *Matrix Biol*. 2014;35:152–161.

60. Wight TN, et al. Versican-A Critical Extracellular Matrix Regulator of Immunity and Inflammation. *Front Immunol*. 2020;11:512.

61. Nakamizo S, et al. Single-cell analysis of human skin identifies CD14+ type 3 dendritic

cells co-producing IL1B and IL23A in psoriasis. *J Exp Med*. 2021;218(9). https://doi.org/10.1084/jem.20202345.

62. Chen Y-L, et al. Re-evaluation of human BDCA-2+ DC during acute sterile skin inflammation. *J Exp Med*. 2020;217(3). https://doi.org/10.1084/jem.20190811.

63. Villani A-C, et al. Single-cell RNA-seq reveals new types of human blood dendritic cells, monocytes, and progenitors. *Science*. 2017;356(6335). https://doi.org/10.1126/science.aah4573.

64. Gregorio J, et al. Plasmacytoid dendritic cells sense skin injury and promote wound healing through type I interferons. *J Exp Med*. 2010;207(13):2921–2930.

65. Li J, et al. Mature dendritic cells enriched in immunoregulatory molecules (mregDCs): A novel population in the tumour microenvironment and immunotherapy target. *Clin Transl Med*. 2023;13(2):e1199.

66. Jiang Y, et al. Cytokinocytes: the diverse contribution of keratinocytes to immune responses in skin. *JCI Insight*. 2020;5(20). https://doi.org/10.1172/jci.insight.142067.

67. Lay K, Kume T, Fuchs E. FOXC1 maintains the hair follicle stem cell niche and governs stem cell quiescence to preserve long-term tissue-regenerating potential. *Proc Natl Acad Sci U S A*. 2016;113(11):E1506–15.

68. Cheng JB, et al. Transcriptional Programming of Normal and Inflamed Human Epidermis at Single-Cell Resolution. *Cell Rep*. 2018;25(4):871–883.

69. Zou Z, et al. A Single-Cell Transcriptomic Atlas of Human Skin Aging. *Dev Cell*. 2021;56(3):383–397.e8.

70. Zhang X, Yin M, Zhang L-J. Keratin 6, 16 and 17-Critical Barrier Alarmin Molecules in Skin Wounds and Psoriasis. *Cells*. 2019;8(8). https://doi.org/10.3390/cells8080807.

71. Lessard JC, et al. Keratin 16 regulates innate immunity in response to epidermal barrier breach. *Proc Natl Acad Sci U S A*. 2013;110(48):19537–19542.

72. Tsuchida S, et al. Characterization of Kdap, a protein secreted by keratinocytes. *J Invest Dermatol*. 2004;122(5):1225–1234.

73. Gandarillas A, Watt FM. c-Myc promotes differentiation of human epidermal stem cells. *Genes Dev*. 1997;11(21):2869–2882.

74. Dai J, et al. The retinoid-related orphan receptor RORα promotes keratinocyte differentiation via FOXN1. *PLoS One*. 2013;8(7):e70392.

75. Dai X, et al. Keratinocyte G2/M growth arrest by 1,25-dihydroxyvitamin D3 is caused by Cdc2 phosphorylation through Wee1 and Myt1 regulation. *J Invest Dermatol*. 2004;122(6):1356–1364.

76. Weddell J. Mechanistically Modeling Peripheral Cytokine Dynamics Following Bispecific Dosing in Solid Tumors. *CPT Pharmacometrics Syst Pharmacol*. [published online ahead of print: January 29, 2023]. https://doi.org/10.1002/psp4.12928.

77. Nazzaro G, et al. Skin manifestations associated with checkpoint inhibitors. *JEADV Clinical Practice*. [published online ahead of print: May 10, 2022]. https://doi.org/10.1002/jvc2.27.

78. Levin AM, et al. Exploiting a natural conformational switch to engineer an interleukin-2 “superkine.” *Nature*. 2012;484(7395):529–533.

79. He H, et al. Single-cell transcriptome analysis of human skin identifies novel fibroblast subpopulation and enrichment of immune subsets in atopic dermatitis. *J Allergy Clin Immunol*. 2020;145(6):1615–1628.

80. Garcia-Diaz A, et al. Interferon Receptor Signaling Pathways Regulating PD-L1 and PD-L2 Expression. *Cell Rep*. 2017;19(6):1189–1201.

880 81. Yang W, et al. PD-L1: PD-1 interaction contributes to the functional suppression of T-cell
881 responses to human uveal melanoma cells in vitro. *Invest Ophthalmol Vis Sci*.
882 2008;49(6):2518–2525.

883 82. Middleton MR, et al. Pharmacodynamic effect of IMCgp100 (TCR–CD3 bispecific) on
884 peripheral cytokines and association with overall survival in patients with advanced
885 melanoma. *J Clin Orthod*. 2019;37(15_suppl):9523–9523.

886 83. Gellatly KJ, et al. scRNA-seq of human vitiligo reveals complex networks of subclinical
887 immune activation and a role for CCR5 in Treg function. *Sci Transl Med*.
888 2021;13(610):eabd8995.

889 84. Crowley LC, Waterhouse NJ. Detecting Cleaved Caspase-3 in Apoptotic Cells by Flow
890 Cytometry. *Cold Spring Harb Protoc*. 2016;2016(11).
891 https://doi.org/10.1101/pdb.prot087312.

892 85. Li B, et al. Fibronectin 1 promotes melanoma proliferation and metastasis by inhibiting
893 apoptosis and regulating EMT. *Onco Targets Ther*. 2019;12:3207–3221.

894 86. Butler MO, et al. Abstract 517: Tebentafusp induces transient systemic inflammation and
895 modifies the micro-environment to sensitize uveal melanoma tumors to cytotoxic CD8 cells.
896 *Cancer Res*. 2021;81(13_Supplement):517–517.

897 87. Leach E, et al. 620 Molecular features in tumors at time of progression on tebentafusp
898 associated with overall survival (OS). *J Immunother Cancer*. 2022;10(Suppl 2).
899 https://doi.org/10.1136/jitc-2022-SITC2022.0620.

900 88. Güç E, et al. Abstract 3289: Melanoma patients with high and low target expression can
901 benefit from TCR-CD3 bispecifics through direct and indirect mechanisms of tumor control.
902 *Cancer Res*. 2023;83(7_Supplement):3289–3289.

903 89. Braud VM, et al. HLA-E binds to natural killer cell receptors CD94/NKG2A, B and C.

Nature. 1998;391(6669):795–799.

90. Maruhashi T, et al. Binding of LAG-3 to stable peptide-MHC class II limits T cell function and suppresses autoimmunity and anti-cancer immunity. *Immunity*. 2022;55(5):912–924.e8.

91. Durante MA, et al. Single-cell analysis reveals new evolutionary complexity in uveal melanoma. *Nat Commun*. 2020;11(1):496.

92. Souri Z, et al. LAG3 and Its Ligands Show Increased Expression in High-Risk Uveal Melanoma. *Cancers* . 2021;13(17). https://doi.org/10.3390/cancers13174445.

93. Phenoptr [Internet]. https://akoyabio.github.io/phenoptr/. Accessed February 26, 2024.

94. Burja B, et al. An Optimized Tissue Dissociation Protocol for Single-Cell RNA Sequencing Analysis of Fresh and Cultured Human Skin Biopsies. *Front Cell Dev Biol*. 2022;10:872688.

95. Solé-Boldo L, et al. Single-cell transcriptomes of the human skin reveal age-related loss of fibroblast priming. *Commun Biol*. 2020;3(1):188.

96. Blanco-Carmona E. Generating publication ready visualizations for Single Cell transcriptomics using SCpubr. *bioRxiv*. 2022;2022.02.28.482303.

97. Fukushi A, et al. Revisited Metabolic Control and Reprogramming Cancers by Means of the Warburg Effect in Tumor Cells. *Int J Mol Sci*. 2022;23(17). https://doi.org/10.3390/ijms231710037.

98. Bassez A, et al. A single-cell map of intratumoral changes during anti-PD1 treatment of patients with breast cancer. *Nat Med*. 2021;27(5):820–832.

99. Liberzon A, et al. The Molecular Signatures Database (MSigDB) hallmark gene set collection. *Cell Syst*. 2015;1(6):417–425.

100. Gene Ontology Consortium, et al. The Gene Ontology knowledgebase in 2023.

927 *Genetics*. 2023;224(1). https://doi.org/10.1093/genetics/iyad031.

928 101. Kanehisa M, et al. KEGG for taxonomy-based analysis of pathways and genomes.
929 *Nucleic Acids Res*. 2023;51(D1):D587–D592.

930 102. Dimitrov D, et al. Comparison of methods and resources for cell-cell communication
931 inference from single-cell RNA-Seq data. *Nat Commun*. 2022;13(1):3224.

932 103. Roederer M. Interpretation of cellular proliferation data: avoid the panglossian.
933 *Cytometry A*. 2011;79(2):95–101.

934 104. Chung S, Lim GJ, Lee JY. Quantitative analysis of melanin content in a three-
935 dimensional melanoma cell culture. *Sci Rep*. 2019;9(1):780.

936 105. Bolaños LV, et al. Glycolytic enzymes lactate dehydrogenase A (LDHA) and
937 phosphofructokinase P (PFKP) are good biomarkers of survival and potential therapeutic
938 targets in cervical cancer. *Ann Oncol*. 2018;29 Suppl 6(suppl_6):vi33.

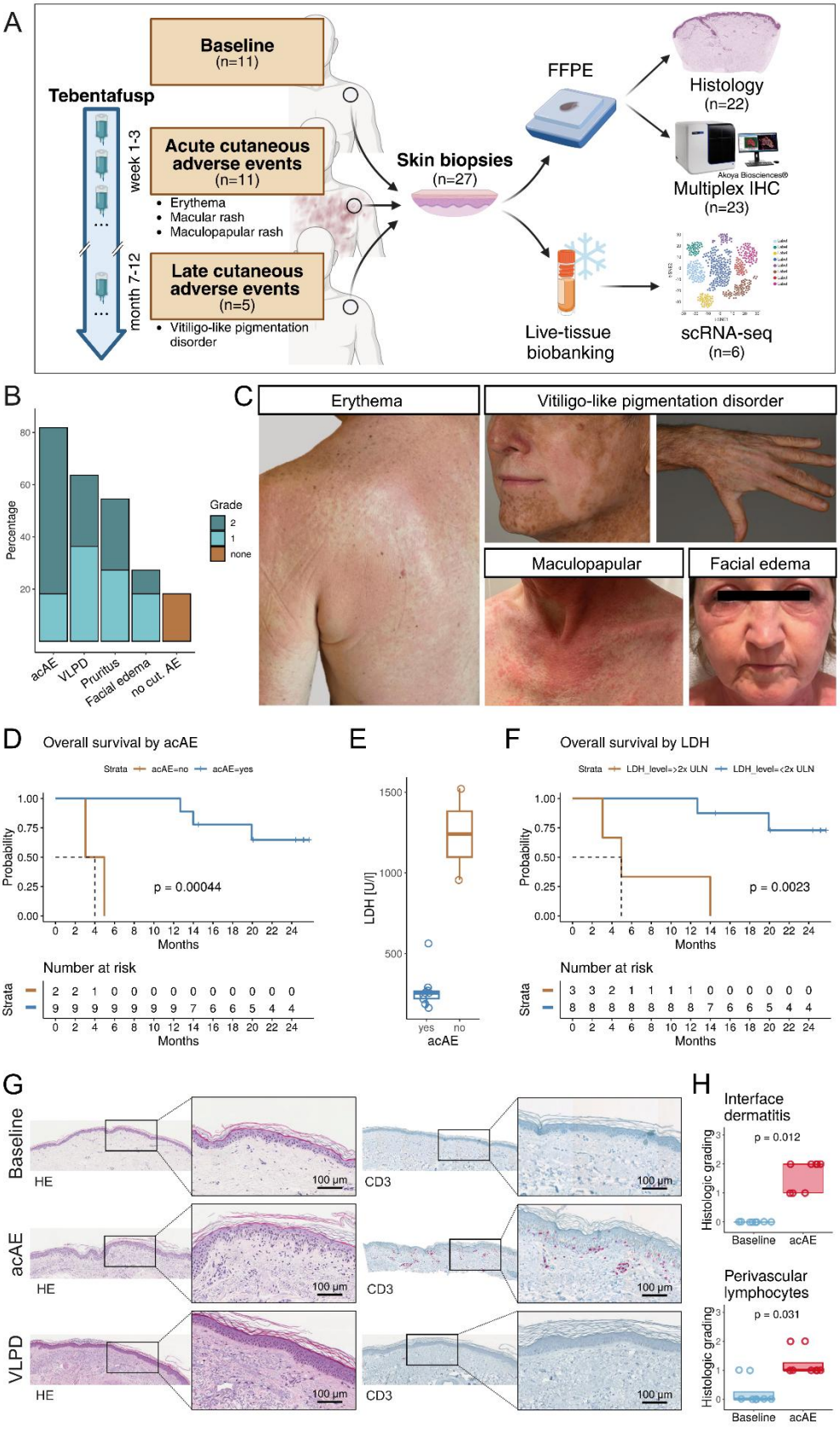

939

940 **Figure 1: Study overview and characterization of clinical cohort.**

A) Overview of experimental design (created with BioRender). **B)** Incidence/grading of cutaneous adverse events (cAE) (n=11). Grading according to CTCAEv5. **C)** Representative clinical photographs of cAE observed under tebentafusp. **D)** Kaplan-Meier curve of overall survival grouped by acAE development (log-rank test). **E)** Baseline LDH levels grouped by acAE development (n=11). **F)** Kaplan-Meier curve of overall survival grouped by baseline LDH levels (log-rank test). **G)** Representative HE and CD3 stainings of baseline, acAE and vitiligo-like pigmentation disorder samples. **H)** Histologic grading of interface dermatitis and perivascular lymphocytes in baseline and acAE (8 patients, paired; Wilcoxon-test).

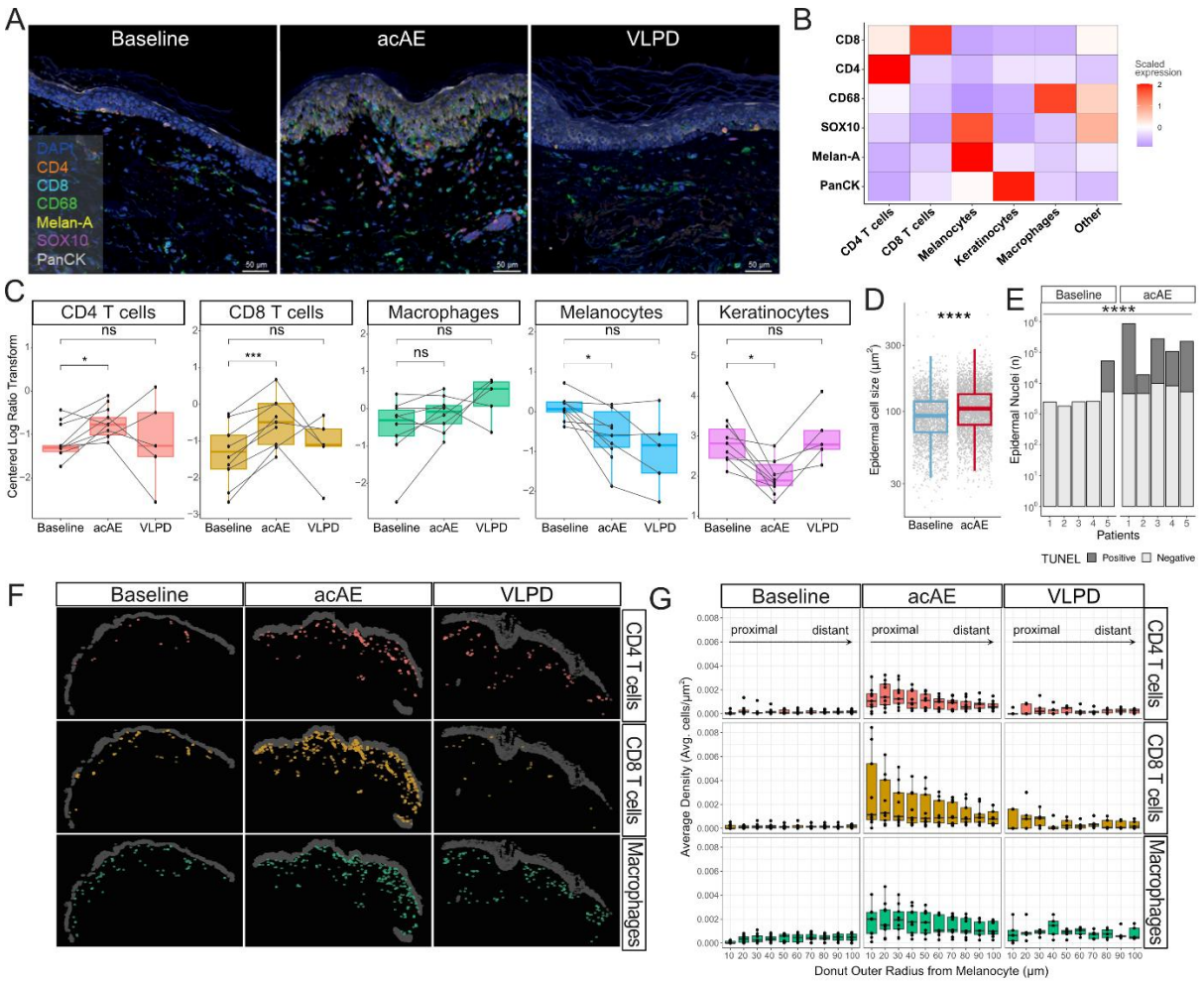

Figure 2: Spatial analysis of cutaneous inflammatory infiltrate on tebentafusp.

A) Representative mIHC scans of baseline, acAE and VLPD skin samples. **B)** Heatmap with scaled marker expression. **C)** Cell type composition at baseline (n=9), acAE (n=9), and VLPD (n=5). Boxplots show the centered-log-ratio transformed cell numbers (t-test). **D)** Epidermal cell sizes at baseline and acAE (n=3, paired; Cohen's d = 0.30). **E)** Epidermal cell death at baseline and acAE skin samples, shown by TUNEL positive and negative epidermal nuclei (n=5, paired). **F)** Representative plot of the spatial distribution of macrophages, CD4+ and CD8+ T-cells, relative to epidermis (gray) at baseline, acAE and VLPD. **G)** Spatial density of immune cells relative to melanocytes at baseline (n=9), acAE (n=9), and VLPD (n=5), ranging from 0 µm (most proximal) to 100 µm (most distant) in 10 µm steps. **: p<0.05 , ***: p<0.001, ****: p<0.0001, ns: not significant.*

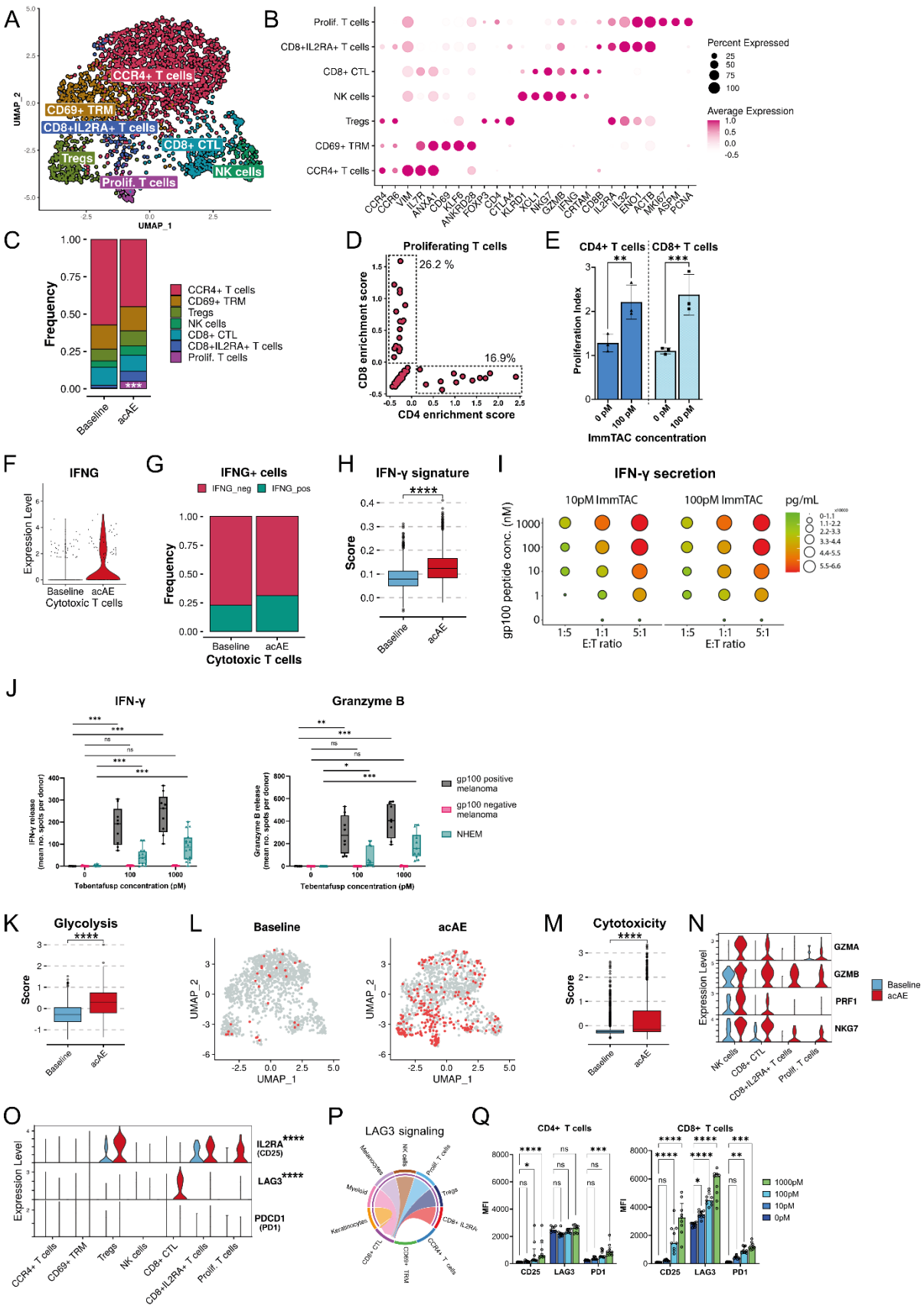

Figure 3: Cytotoxic T-cell activation and LAG3 upregulation in response to tebentafusp.

A) UMAP of T/NK cell subclusters in integrated baseline (1343 cells) and acAE (1175 cells) skin samples (n=3, paired). **B**) Marker gene dotplot and **C**) cell type composition barplot (Exact test). **D**) Feature scatter plot showing the percentage of CD4 and CD8A/CD8B expressing cells. **E**) Proliferation index of CD4+ and CD8+ T-cells after co-culturing with gp100+ cells, with/without gp100-ImmTAC (ANOVA). **F**) Violin plot of IFNG expression. **G**) Frequency of IFNG positive CTLs. **H**) Boxplot showing the IFN-γ gene signature (99) in T/NK cells (Wilcoxon rank-sum test). **I**) Dotplot of IFN-γ protein concentrations in the supernatant of T-cells co-cultured with gp100-peptide-pulsed T2 cells in gp100-ImmTAC presence at different effector-target ratios. **J**) In vitro activity of tebentafusp against skin melanocytes. PBMC and CD8 T-cells used as effector cells in IFN-γ and Granzyme B in ELISpot assays, respectively (t-test). **K**) Boxplot and **L**) Feature plot showing the glycolysis gene signature in T/NK cells (Wilcoxon rank-sum test). **M**) Boxplot of the cytotoxicity signature in T/NK cells (Wilcoxon rank-sum test). **N**) Violin plot showing the cytotoxic signature expression in T-cell subclusters. **O**) Violin plot showing IL2RA, LAG3 and PDCD1 in T/NK subclusters (Wilcoxon rank-sum test). **P**) Chord diagram showing inferred LAG3 signaling in acAE between cell types. **Q**) CD25, LAG3 and PD1 protein levels in CD4+ and CD8+ T-cells after co-culturing with gp100+ cell line at increasing gp100-ImmTAC concentrations (ANOVA).

: p<0.05 ,: p<0.01, ***: p<0.001, ****: p<0.0001.*

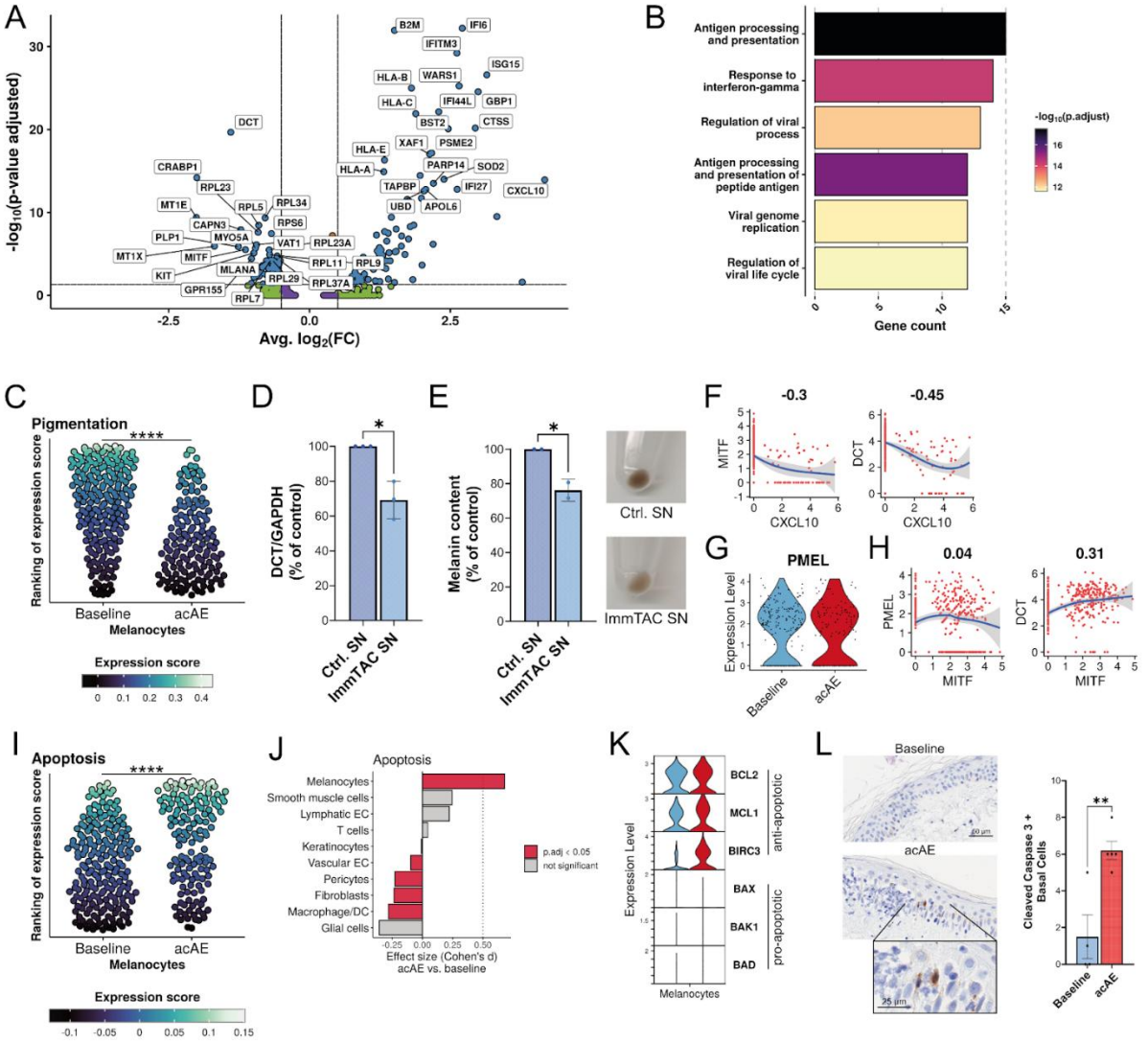

Figure 4: IFN-γ responses and apoptosis in melanocytes.

A) Volcano plot showing differential gene expression of melanocytes in acAE versus baseline skin samples (cut-offs: p-adj<0.05, |log2FC|>0.5) **B)** Gene ontology pathway enrichment of upregulated genes in melanocytes of acAE versus baseline skin. **C)** Bee-swarm plot showing the pigmentation gene signature (100) in melanocytes (Cohen's d = 0.78) (Wilcoxon rank-sum test). **D)** Normalized DCT protein levels in melanocytes treated with gp100-ImmTAC co-culture supernatant versus control, quantified by WB (n=3) (t-test). **E)** Melanin content of melanocytes treated with supernatant derived from gp100-ImmTAC co-culture experiments versus control supernatant, quantified by photometric absorbance (n=2) (t-test). **F)** Correlation of *MITF* and *DCT* expression with *CXCL10* in melanoytes (Pearson correlation). **G)** PMEL expression in baseline and acAE melanocytes. Not significant. **H)** Correlation of *MITF* with *PMEL* and *DCT* expression in melanocytes (Pearson correlation). **I)** Bee-swarm plot showing the apoptosis gene signature (KEGG, in melanocytes (Cohen's d = 0.61) (Wilcoxon rank-sum test). **J)** Barplot showing the effect size (Cohen's *d*) and the direction of up- or downregulation of the apoptosis gene signature (101) in acAE versus baseline skin (Wilcoxon rank-sum test). **K)** Violin plot showing the expression of

anti- and pro-apoptotic genes in melanocytes. **L)** Representative cleaved caspase 3 staining and quantification of positive cells in the basal epidermis (n=5, paired) (t-test). *SN: Supernatant. *: p<0.05 ,**: p<0.01, ***: p<0.001, ****: p<0.0001.*

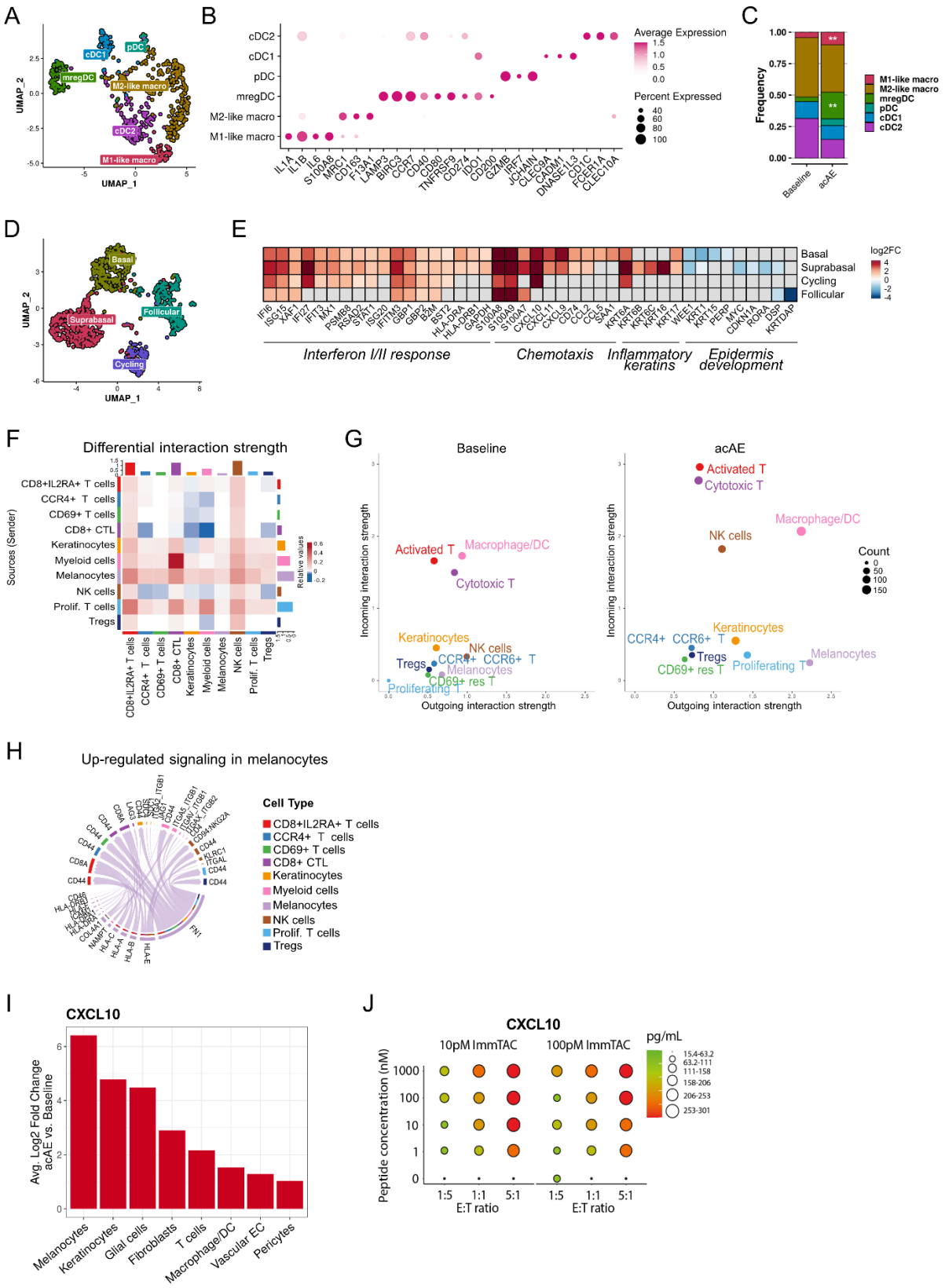

Figure 5: Network of pro-inflammatory and immuno-regulatory functions in bystander cells.

A) UMAP of myeloid cell subclusters in integrated baseline (254 cells) and acAE (331 cells) skin samples (n=3, paired). **B)** Marker gene dotplot and **C)** cell type composition barplot of myeloid cell subclusters. Asterisks indicates

significantly differentially abundant subclusters. **D)** UMAP of keratinocyte subclusters in baseline and acAE skin samples (n-3, paired). **E)** Heatmap of differentially expressed genes in the keratinocytes of acAE versus baseline according to subcluster. Genes are grouped by biological function and significant differences are colored by log2 fold-change. **F)** Heatmap of differential interaction strength in cell-cell communication between indicated cell types in acAE versus baseline skin (CellChat). **G)** Outgoing and incoming signal strength according to cell type (CellChat). **H)** Chord diagram showing the upregulated signaling pathways from melanocytes to other cell types (CellChat). **I)** Log2fold change of *CXCL10* expression in acAE versus baseline skin.. **J)** Dotplot of CXCL10 protein concentrations in the supernatant of T-cells co-cultured with gp100-peptide pulsed T2 cells (gp100 ranging from 0-1000 nM) in gp100-ImmTAC presence (10/100 pM) at different effector-target ratios, **: p<0.05 ,**: p<0.01, ***: p<0.001, ****: p<0.0001.*

Supplementary Tables

Supplementary Table 1: Skin-related information.

Patient	Sex	Age	Cutaneous adverse events	Follow-up skin biopsy	Biopsy from vitiligo-like pigmentation disorder	Assays
1	m	58	Diffuse erythema, pruritus, vitiligo-like pigmentation disorder	Day 15	Month 7 (tebentafusp treatment ongoing)	scRNA-seq mIHC histology
2	m	74	Diffuse erythema, pruritus, vitiligo-like pigmentation disorder	Day 8	Month 12 (tebentafusp treatment ongoing)	scRNA-seq mIHC histology
3	f	62	Diffuse erythema, macular exanthema, facial edema, pruritus, vitiligo-like pigmentation disorder	Day 2		scRNA-seq mIHC histology
4	m	57	Maculopapular exanthema, partly diffuse erythema on face and neck, vitiligo-like pigmentation disorder	Day 2	Month 8 (tebentafusp treatment ongoing)	mIHC histology
5	m	66	Diffuse erythema, pruritus, vitiligo-like pigmentation disorder	Day 15	Month 9 (tebentafusp treatment ongoing)	mIHC histology
6	m	56	Diffuse erythema, vitiligo-like pigmentation disorder	Day 8	Month 7 (tebentafusp treatment ongoing)	mIHC histology
7	f	47	Diffuse erythema, single fluid-filled vesicle	Day 17		mIHC histology
8	f	67	Diffuse erythema, pruritus	Day 1		mIHC histology
9	m	66	Diffuse erythema, hand and facial edema, vitiligo-like pigmentation disorder	Day 8		mIHC
10	m	67	None	Day 14		histology

11	m	62	None	Day 8		histology

m: male, f: female, scRNA-seq: single cell RNA-sequencing, mIHC: multiplex immunohistochemistry

Supplementary Table 2: Tumor-related information

Patient #	Sex	Age	Uveal melanoma disease stage	Site of metastases	Previous treatments	Cytokine-release syndrome (CRS) on tebentafusp	Treatment of CRS
1	m	58	Stage IV	Lymph nodes, liver, bone, retroperitoneal space, pleura	Dacarbazine, Ipilimumab/Nivolumab, Temozolamid, Denosumab	CRS grade 2	fluids, paracetamol, metamizole, morphine
2	m	74	Stage IV	Liver	Ipilimumab/Nivolumab	CRS grade 2	fluids, paracetamol, metamizole
3	f	62	Stage IV	Liver, lung	Pembrolizumab, Temozolamid, Ipilimumab/Nivolumab	CRS grade 2	fluids, paracetamol, metamizole
4	m	57	Stage IV	Liver	none	CRS grade 2	fluids, paracetamol
5	m	66	Stage IV	Liver	Ipilimumab/Nivolumab	CRS grade 1	paracetamol, metamizole
6	m	56	Stage IV	Liver, lymph nodes	none	no CRS	none
7	f	47	Stage IV	Liver, bone	none	CRS grade 2	fluids, ibuprofen
8	f	67	Stage IV	Liver	none	no CRS	none
9	m	66	Stage IV	Liver	none	no CRS	none
10	m	67	Stage IV	Liver, brain, lymph node, pleura, pericardium, lung, muscle, thyroid, pancreas, colon, abdominal soft tissue, kidney, bone	Ipilimumab/Nivolumab, Temozolamid, Mekinist, Denosumab	CRS grade 1	paracetamol, metamizole
11	m	62	Stage IV	Liver, lung, lymph node, subcutaneous tissue, muscle	Ipilimumab/Nivolumab, Temozolamid, Pembrolizumab, Lenvatinib, Carboplatin	CRS grade 1	paracetamol, domperidone

CRS: Cytokine-release syndrome (according to CTCAE v5)

Supplementary Table 3: Vitiligo-like pigmentation disorder

Patient	Fitzpatrick Phototype	Distribution pattern of VLPD	Signs of activity (trichrome, confetti)	Diagnosis of VLPD	Biopsy timepoint	Biopsy site	VLPD dynamic at time of biopsy
1	IV	Generalized, symmetrical,	confetti and trichrome	Month 3	Month 7	Upper arm	Expanding

		mottled with confluent patches. Generalized leukotrichia.					
2	III	Generalized, symmetrical, mottled. Generalized leukotrichia.	confetti	Month 9	Month 12	Lower arm	Stable
4	II	NA	confetti	Month 6	Month 8	Lower arm	Stable
5	III	Leukotrichia of eye brows and lashes.	confetti	Month 7	Month 9	Face	Expanding
6	II	Generalized, symmetrical, mottled with confluent patches. Generalized leukotrichia.	confetti	Month 5	Month 7	Face	Expanding

VLPD: vitiligo-like pigmentation disorder

Supplementary Figures

Supplementary Figure 1

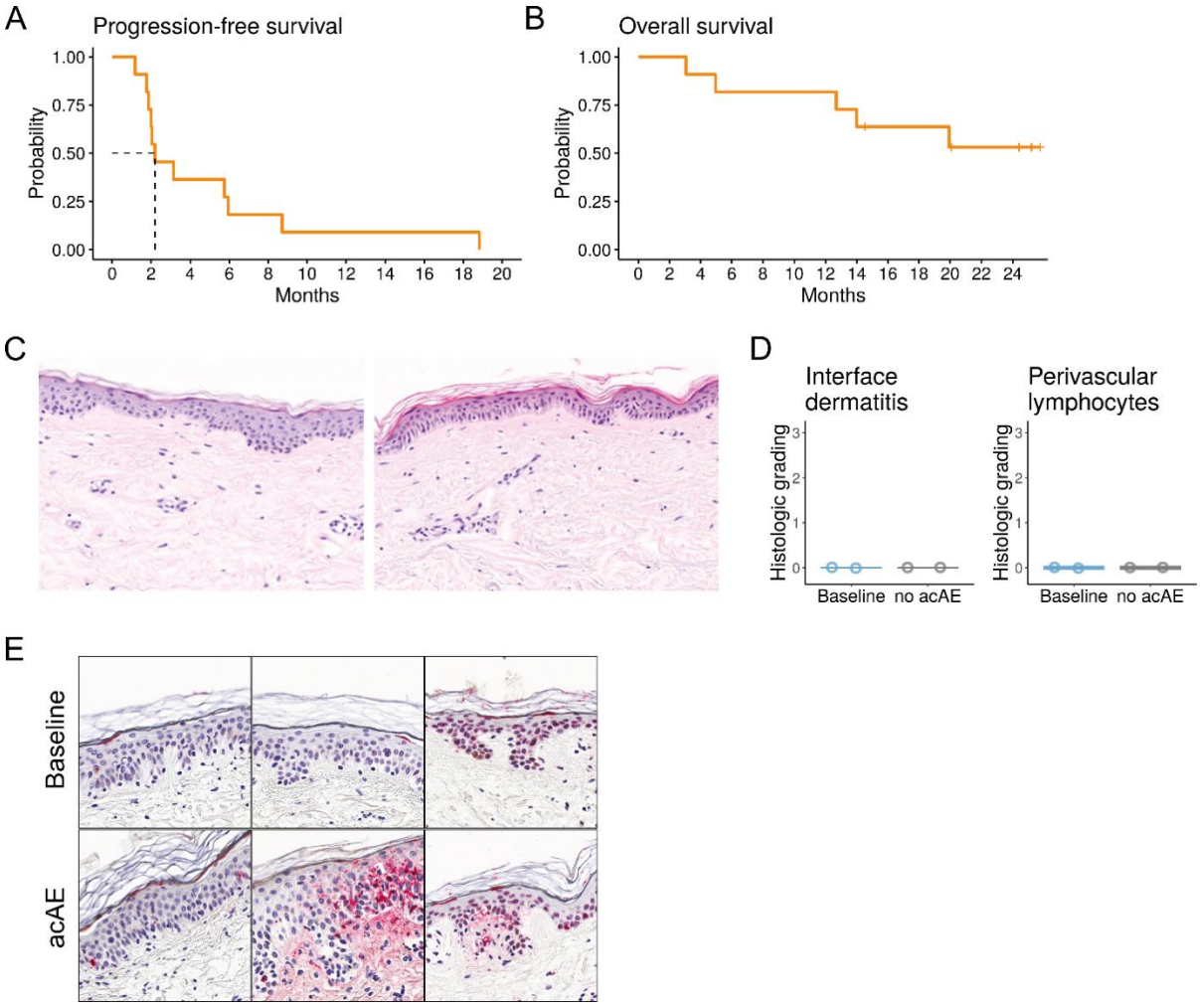

A) Kaplan-Meier curve of progression-free survival (PFS) and **B)** overall survival of patients with uveal melanoma treated with tebentafusp (n=11). Tick marks indicate censoring. **C)** Representative histology images of on-treatment skin biopsies from patients without acAE. **D)** Histologic grading of interface dermatitis and perivascular lymphocytes in baseline and non-acAE on-treatment skin samples (2 patients, paired). **E)** Representative TUNEL (Terminal deoxynucleotidyltransferase mediated dUTP Nick End Labeling) staining of baseline and acAE skin samples.

Supplementary Figure 2

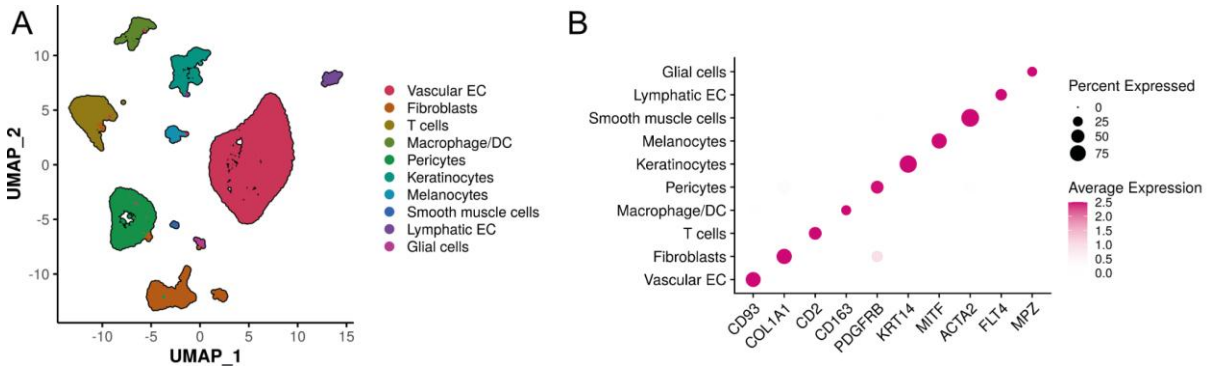

A) UMAP representation of all cell types in integrated baseline and acAE skin samples analyzed by single cell RNA-sequencing (3 patients, paired). **B)** Dotplot of lineage marker expression.

EC: Endothelial cells

Supplementary Figure 3

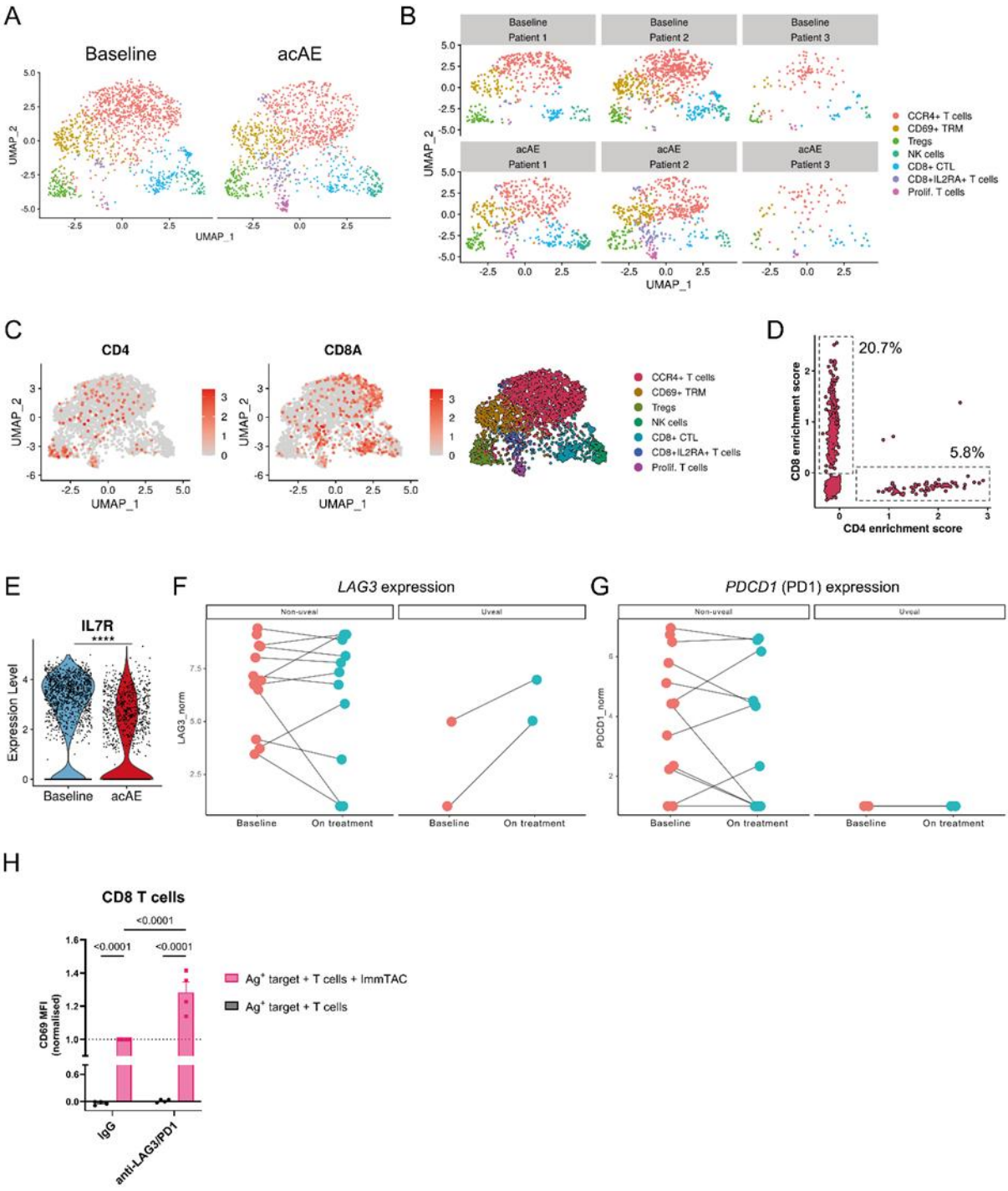

A) UMAP of T and NK cell subclusterss split by timepoint. **B)** UMAP split by timepoint and patient. **C)** UMAP feature plot showing CD4 and CD8A expression. **D)** Feature scatter plot showing the percentage of CD4 and CD8A/CD8B expressing cells in the CCR4+ T cell subcluster. **E)** Violin plot of IL7R

expression in T and NK cells on scRNA-seq. **F)** Log2-normalized expression of *LAG3* and **G)** *PDCD1* (PD1) in baseline and on treatment tumor biopsies from patients with uveal (n=2) or non-uveal (n=11) melanoma treated with tebentafusp, derived from a published RNA dataset (*Middleton, M.R., et al. (2020). Tebentafusp, A TCR/Anti-CD3 Bispecific Fusion Protein Targeting gp100, Potently Activated Antitumor Immune Responses in Patients with Metastatic Melanoma. Clin. Cancer Res. 26, 5869–5878.).* **H)** CD8 T cell activation as measured by CD69 when co-cultured with antigen expressing target cells with or without ImmTAC and anti-LAG3/anti-PD1 antibodies or IgG isotype control.

Ag: Antigen

Supplementary Figure 4

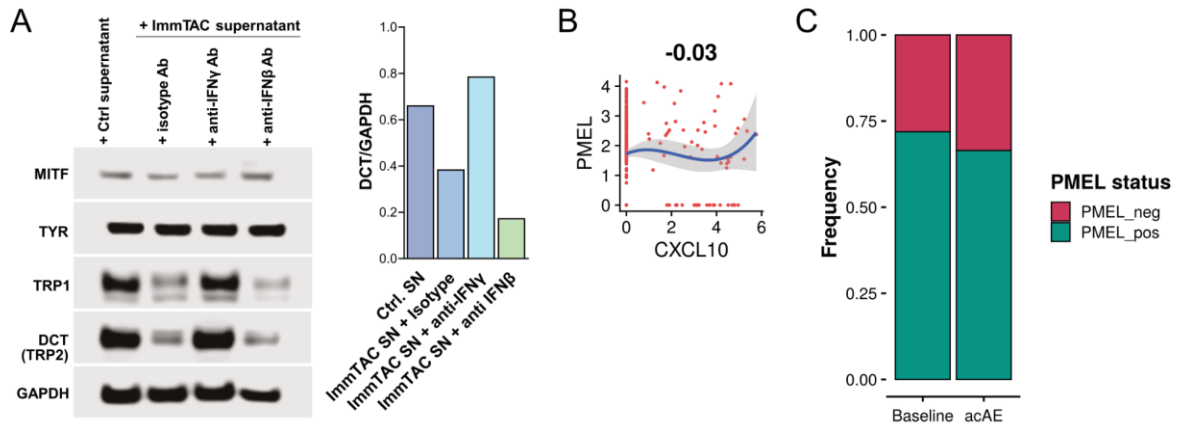

A) WB of the melanocytic proteins MITF (Melanocyte Inducing Transcription Factor), TYR (Tyrosinase), TRP1 (Tyrosinase Related Protein 1), and DCT (Dopachrome Tautomerase) derived from melanocytes treated with supernatant derived from gp100-ImmTAC co-culture experiments with the addition of an isotype control, anti-IFN-γ, or anti-IFN-β antibody. The normalized DCT values are shown as barplots. **B)** Correlation of *PMEL* and *CXCL10* expression levels in melanocytes on scRNA-seq. Pearson correlation is indicated. **C)** Frequency of *PMEL*-positive melanocytes on scRNA-seq.

Ctrl: Control, Ab: Antibody, ImmTAC: Immune Mobilizing Monoclonal T cell Receptor Against Cancer, GAPDH: Glyceraldehyde-3-Phosphate Dehydrogenase, SN: Supernatant, acAE: acute cutaneous adverse event

Supplementary Figure 5

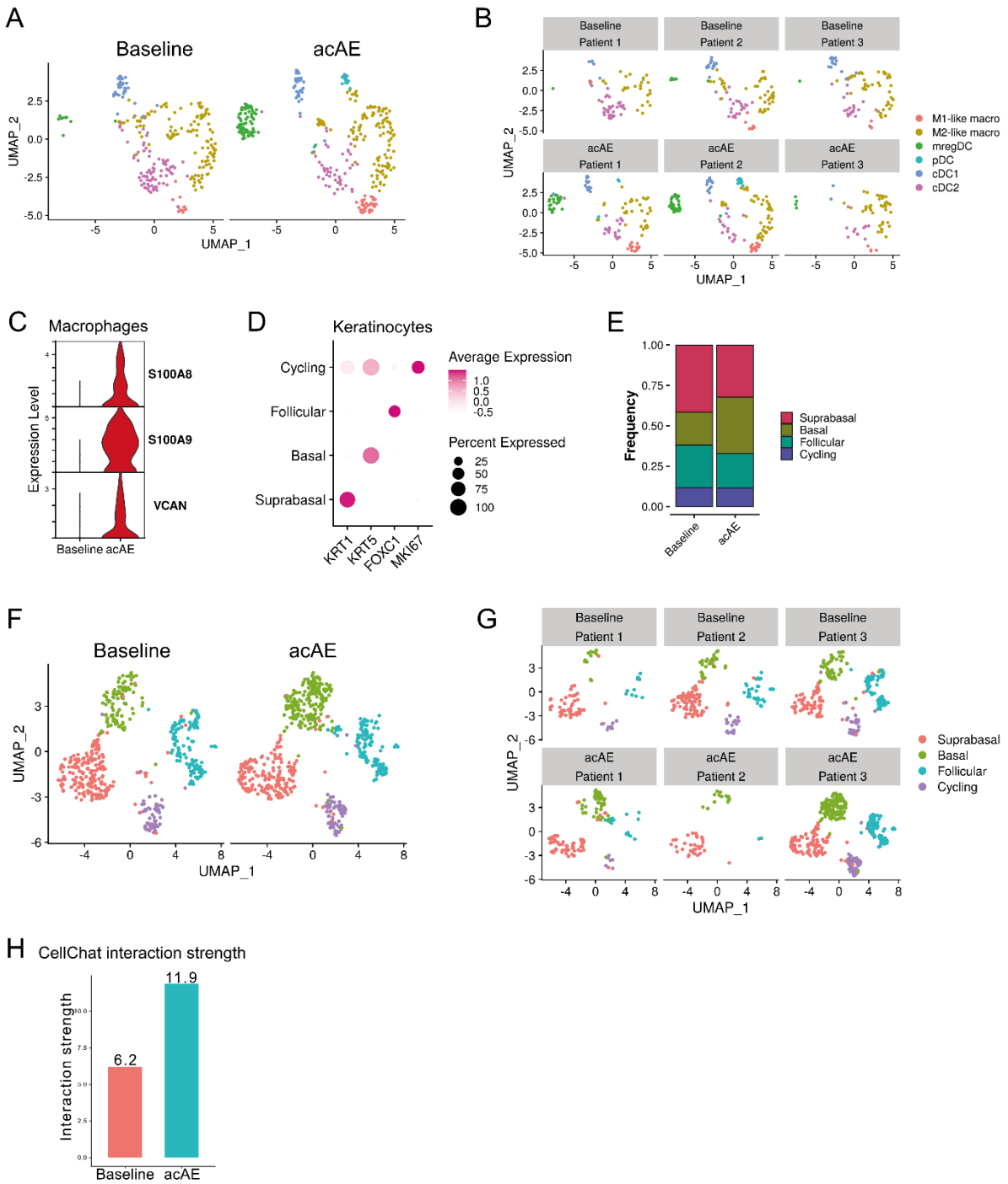

A) UMAP of myeloid cell subclusters split by timepoint and **B**) split by timepoint and patient. **C)** Violin plot of *S100A8*, *S100A9* and *VCAN* expression in macrophages on scRNA-seq. **D)** Marker gene dotplot and **E)** cell type composition barplot of keratinocyte subclusters on scRNA-seq. **F)** UMAP of keratinocyte subclusters split by timepoint and **G)** split by timepoint and patient. **H)** Cell-cell communication interaction strength as inferred from CellChat analysis.

acAE: acute cutaneous adverse event, cDC1: classical dendritic cell type 1, cDC2: classical dendritic cell type 2, mregDC: mature DC enriched in immunoregulatory molecules, pDC: plasmacytoid DC